PCCP

ROYAL SOCIETY OF CHEMISTRY

TUTORIAL REVIEW

View Article Online
View Journal | View Issue

Cite this: *Phys. Chem. Chem. Phys.*, 2025, **27**, 19591

Electrical XPS meets biology: *in situ* chemo-electrical sensing and activation of organic materials

Marco E. Miali,[a] Ulyana Shimanovich [a] and Hagai Cohen *[b]

Received 28th November 2024,
Accepted 30th June 2025

DOI: 10.1039/d4cp03762f

rsc.li/pccp

X-ray photoelectron spectroscopy (XPS) is a popular analytical technique in materials sciences owing to its versatile coverage of broad energy ranges and the reliability of its quantitative compositional analysis. Hence, tailoring XPS capabilities to the research frontiers of biological systems and nature-inspired materials can potentially be of great value. However, the application of XPS in bio/organic systems encounters critical inherent challenges, specifically amplified by the rich nuances that are at the heart of biological functions. The present mini review describes some of these difficulties, showing that by combining electrical-sensing capabilities *in situ* with standard XPS chemical analysis, diverse and effective solutions can be achieved. A related method, termed chemically resolved electrical measurements (CREM), is described, and case study examples are provided, ranging from self-assembled monolayers of small molecules to relatively large supramolecular sugars and proteins. A detailed discussion is dedicated to specimen stability issues, charge capturing and hot-charge transport functionalities, for which the CREM approach provides particularly attractive capabilities and a template for advanced characterization strategies.

1. Introduction

Nature-inspired materials can exhibit impressive multifunctional properties, which evolved through precise hierarchical structural organization.[1–3] Such natural architectures possess the desirable ability to integrate the properties and characteristics of their individual components in an intelligent hierarchical design, which usually surpasses the sum of their individual parts in terms of efficiency and energy optimization. Thus, the successful construction of artificial nature-mimicking materials can be achieved only when valuable information on the structural characteristics of individual building blocks, the type of dominant interfacial interactions between the components and the mesoscale behavior of homogeneous and heterogeneous composites is acquired.[4] Then, the structural, mechanical and electrical properties may be flexibly tuned by, for example, changing the synergistic characteristics of interfacial interactions. The latter approach has been recently established as a revolutionary concept for fabricating sustainable, mechanically stable and electrically sensitive functional materials made of natural building blocks.[5,6]

Can the standard techniques of material research be effective with bio-related derivatives? Apparently, some of the properties commonly used for the characterization of condensed matter architectures are by far less relevant in the case of biological samples. For example, the crystalline order probed using X-ray diffraction (XRD) can hardly account for the hierarchical, functionally guided types of orders in biological systems. Extended electronic states governed into energy bands, as commonly realized in condensed matter physics, would normally be replaced in organic molecules by nanometer-scale localized orbitals. These and other properties impose major differences on the effectivity of characterization tools, frequently encountering conceptually different approaches in the theoretical models of their analysis. There have been continuous attempts to bridge the related methodological gaps in system analysis, exploiting, for example, the growth of organic crystals for XRD,[7,8] the attachment of markers for optical measurements,[9] and rapid freezing for cryo-electron microscopy of soft tissues.[10,11] However, the development of new tools that are sensitive enough and sufficiently flexible to capture the rich structural and functional nuances in biological systems is still of great demand.

Among the effective characterization means, X-ray photoelectron spectroscopy (XPS) is a well-established technique for chemical analyses of surfaces.[12–15] It proposes reliable quantification of atomic concentrations and surface

[a] *The Department of Molecular Chemistry and Materials Science, The Weizmann Institute, Rehovot 76100, Israel*
[b] *The Department of Chemical Research Support, The Weizmann Institute, Rehovot 76100, Israel. E-mail: hagai.cohen@weizmann.ac.il*

stoichiometry,[16,17] combined with fine resolution of elemental oxidation states and, added to those, a remarkable, sub-nanometer scale, depth resolution in the compositional analysis. Together with a continuous progress in establishing improved energy resolution and mapping capabilities,[18–20] XPS has become very popular in materials research and surface science studies.[21–23]

Besides its well-acknowledged chemical analytical capabilities, access to electrical information is inherent to the XPS technique, simply because it is based on the spectroscopy of charged particles: electrons. Unfortunately, the photoemission process itself involves loss of charge neutrality and, consequently, sample charging can gain large magnitudes in insulating samples (normally, positive charge). The accumulated charge affects the energy of outgoing electrons and, thus, a two-fold problem is encountered: On the one hand, the input beam modifies the sample electrically and, on the other hand, at the detection side, the spectroscopy is extremely sensitive to those changes. As a result, charging related spectral distortions have become a routine issue of concern in XPS studies.[24–26] In particular, the non-uniform distortions, termed 'differential charging', can severely smear the information on oxidation states and, in extreme cases, even confuse the basic elemental analysis. Notably, however, these very effects were also shown to provide a source of rich and useful information.[27–32]

In order to minimize the charging-related artifacts, a neutralizer is commonly used, *i.e.* an electron flood gun (eFG) that sprays low-energy electrons on the surface such as to compensate for the accumulation of positive charge. This eFG is also capable of forming (on purpose) extra negative charging and, thus, be used to controllably stabilize the surface charge and establish a template for electrically driven experiments, making use of the artifact instead of fighting it.[30,33,34] These attempts have led to the development of a technique that focuses on XPS-based derivation of electric information, termed chemically resolved electrical measurements (CREM). Conceptually, the problem of charging has been generalized to treat the experimental setup as an electrical system in its broadest sense.[35–38] CREM is not necessarily orthogonal to other XPS approaches. Its contribution *via* systematic inspection of the electric information can in principle be combined with other XPS-based modes like near ambient pressure (NAP)-XPS or Cryo-XPS. A number of unique capabilities as compared to any of the standard electrical tools have thus been demonstrated and the combined chemical & electrical information has become very powerful in studies of a variety of systems. Among its noticeable features, CREM proposes: (1) no need in top contacts for the electric measurement; (2) by exploiting elemental addresses, it is capable of resolving electrical characteristics at selected subsurface domains; and (3) unique sensitivity to hot-electron characteristics is achieved.[39]

Specifically, in surface organic chemistry, the application of CREM promises a remarkable feature: Atomic resolution of the electric data can be approached (probed by a macroscopic tool), based on local potentials extracted from selected atomic addresses.[40–42] This feature is particularly attractive, recalling that standard electrical measurements at the sub-molecular level are nearly impossible. Except for difficulties in forming reliable contacts, a fundamental difficulty is encountered by the standard techniques: electrical measurements are generally limited to detect signals from the integral volume between attached electrodes. Hence, detecting electrically and directly a specific atomic site in a molecule is extremely difficult. In this context, remarkable reports on SPM-based studies at selected molecular sites should be noted.[43–46] In turn, with a relatively simple experimental setup and a top-contact-free configuration, CREM can easily resolve such information from uniform molecular layers.

As such, the motivation for exploiting XPS in studies of organic systems is clear. However, major XPS limitations, specifically enhanced with organic and bio-molecules, turn the experiment highly challenging.[47,48] In the present review, these difficulties are discussed together with a brief review on XPS-based experiments performed in our laboratory. No attempt is made here to cover the entire field, but instead use specific experiments as examples in which difficulties were successfully addressed and, in most cases, new and valuable information could be harvested.

The following sections start with a list of major obstacles encountered upon XPS application to organic and bio materials (section 2). A dedicated introductory section on the CREM technique is given as well (section 3), including (i) a concise presentation of the theoretical model for CREM current–voltage characteristics and (ii) comparison to other techniques. These introductory parts are followed by a set of case-studies, with which unique aspects of the electrical-XPS in its application to organic specimens are exemplified, including: the remarkable CREM sensitivity as a probe of sample damage (sections 4.1 and 4.2); experiments exploiting beam-damage as a writing means (section 4.3); light-induced charge transport mechanisms across self-assembled monolayers (SAMs), section 5.1; probing non-trivial SAM packing forms and defect evolution processes, section 5.2; 'sophisticated' structure-function relationships that are broadly exploited in nature and XPS-revealed at monolayers of bacteriochlorophyll derivatives (section 6); intriguing electrical characteristics upon incorporating macro-protein molecules at the core-junction of transistor devices (section 7); ion diffusion in pectin (section 8); and the electrically-assisted XPS-based evaluation of hydrogen bonds (section 9). A summary of the subject is provided as well (section 10).

2. Obstacles in XPS application to biomaterials

It turns out that some of the broadly acknowledged advantages of XPS become ineffective, or at least less effective, when applied to organic and biological compounds. This section discusses some of the major obstacles encountered in XPS applications to organic molecules and bio-materials in particular.

1. While XPS can effectively quantify atomic concentrations of key elements such as C, O, N, S, K and others, it is essentially blind to hydrogen (H). Hydrogen, as a major constituent of the organic matrix, is of great importance in the molecular structure, interactions, properties and activity. Therefore, the fact that XPS is incapable of direct H-sensing is by any means a severe drawback of the technique.
2. The H-detection problem is further amplified by the poor XPS resolving power of carbon states at finely different C–H and C–C bonding. Such states would usually reflect conformational variations that constitute biological richness and, frequently, are of great importance. Again, the limited XPS spectral capabilities in this matter present a severe drawback.
3. Independent of the above-mentioned probe limitations, an issue concerning the sample itself is common to XPS studies of soft matter: the sample stability.[49,50] First, as XPS is conducted under ultra-high vacuum (UHV), evaporation of small molecular species is commonly encountered, dehydration in particular, initiated as soon as the vacuum pumps are switched on. This problem is further enhanced upon exposure to the X-ray source, namely to the ionizing irradiation. As exemplified below, loss of materials during XPS measurements is likely to induce conformational and property changes, to which our probe may be badly insensitive, with poor ability to even identify the 'problem'.
4. Damage processes that do not involve evaporation are also expected to be induced by the X-ray irradiation. The photon energy in XPS is selected such as to be sufficiently high for ejecting core electrons. Therefore, as an unavoidable byproduct, the strong perturbation encountered upon core-electron excitation tends to result in complex relaxation processes, including bond breaking and rearrangement of atoms.
   Attempts to address these difficulties include the development of cryo-XPS,[51,52] by which degradation processes can be slowed down drastically. Near-ambient pressure (NAP)-XPS,[53–55] in which nearly atmospheric pressure is retained just above the sample, is also relevant in this context. Each of these approaches introduces specific difficulties that will not be discussed here. Instead, focus is put on the improvement of probe sensitivity to the emergence of irreversible sample modifications, such that derivation of 'damage-free' data can be approached and corresponding experimental protocols be developed. Moreover, as a further step, works exploiting the beam-induced modifications as fine 'writing' tools are described.
5. As already mentioned, charging effects introduce notable difficulties to the XPS analysis. Unfortunately, many of the organic and bio-related specimens present features that magnify these difficulties. First, organics are frequently very poor conductors, hence subjected to enhanced charging. Second, in many cases, the sample morphology is far from being evenly planar. Fibers,[6,56–58] micelles[59,60] and others would normally form highly irregular surfaces such that differential charging is likely to evolve and introduce pronounced spectral distortions to the XPS analysis. Whether the neutralizer is activated or not, the already limited resolving power of molecular conformational states may then become totally irrelevant to the actual research needs.
6. To make a problem even harder, the application of a neutralizer, namely sending a flux of charged particles directly to the surface, would likely accelerate part of the damage processes while, as previously explained, the XPS probe may be rather insensitive to their occurrence. The reduction of metal ions[61] in metal–organic systems is an example of processes that, indeed, are likely to be inspected by XPS and, yet, confusion may arise if the amount of charge deposited by the XPS probe is not taken into account (see, for example, recent reports on cryptoelectrons, claimed to be created under tribo-experiments with insulating polymers such as Teflon and PMMA).[62–65]
7. Finally, a note may be added on the spatial resolution presently available by XPS spectrometers. It is well known that XPS presents an interesting case of fantastic surface sensitivity together with very poor lateral resolution. The superior surface sensitivity turns into a problem when regimes of interest are located at sub-surface domains, *e.g.* a few tens of nanometers below surface, which is usually the situation for biological specimens. In condensed matter analyses, Ar-ion sputtering is a popular means for digging-in and exposing new (sub-surface) domains to the surface sensitive probe.[66,67] With soft tissues, the sputtering process is likely to be too aggressive, even if gentle sputtering by Ar-clusters is used.[68,69] It introduces critical unknowns upon limited conformational stability, which is so common to soft matter specimens and, in addition, differential sputtering artifacts are likely to appear.
   As of lateral dimensions, in best cases the XPS spatial resolution approaches the micrometer scale, requiring then higher exposures, and hence accelerated damage. Besides the trivial disadvantage of large area analyses, bio-systems frequently consist of spatial variations in composition and properties across hierarchical length scales. Therefore, one may encounter the intermediate situation of having neither site-selectivity nor reliable averaging by the acquired data.

The above partial list of difficulties in XPS application to biomaterials is fully supported by the experience gained in our laboratory. It may be suspected that related literature has remained insufficient as a result of probe insensitivity to these very processes and products. Therefore, it should be stressed that *in situ* integration of CREM along with the standard XPS gains invaluable improvements. As shown below, CREM is very efficient in the identification of emerging damage processes. Second, it proposes significantly better elimination of the charging artifacts and, thus, enables improved quality of the bare XPS data. Relatedly, CREM-based differentiation between spatial domains,[31,33] especially regarding their vertical arrangement and compositional contrast,[34] is of great help for the standard XPS interpretation and quantification, because signal intensities depend on depth-determined attenuation factors. On top of those, beyond the 'XPS-related' improvements, added values are gained by opening a whole new dimension of information

that can be harvested: the electrical properties of samples. Finally, some of the latter CREM capabilities were found to be unique as compared to any of the standard electrical probes. Remarkably, CREM can even extract partial information from macro-deep domains, far deeper than the escape-depth of photoelectrons. Then, part of the unique CREM capabilities are indeed lost, but not all. As such, the combined CREM-XPS technique can potentially open exciting doors towards learning about the functionalities of systems.

3. The CREM technique

3.1. General description

In this section, a brief introduction to the CREM technique is provided. A schematic illustration of the experimental setup is shown in Fig. 1a, explaining the variety of signal-in and signal-out means. CREM exploits the fact that electron spectroscopy, in contrast to optical spectroscopy, is inherently sensitive to variations in the electrostatic potential at sites of photoelectron emission.[30,35] In fact, this is the very origin of chemical shifts that are at the heart of the XPS analysis. Commonly, the term 'chemical shift' in its XPS context refers to changes in the charge density around atomic cores as a result of chemical bond formation. However, changes in the electrostatic potential at a given site can also be induced by distant charges, even by macroscopically distant ones. Therefore, it would be convenient to treat the peak-energy information as a combination of two components, a chemical and an electrostatic one, referring, respectively, to the local (atomic scale) charge density and, to be distinguished from the former, a

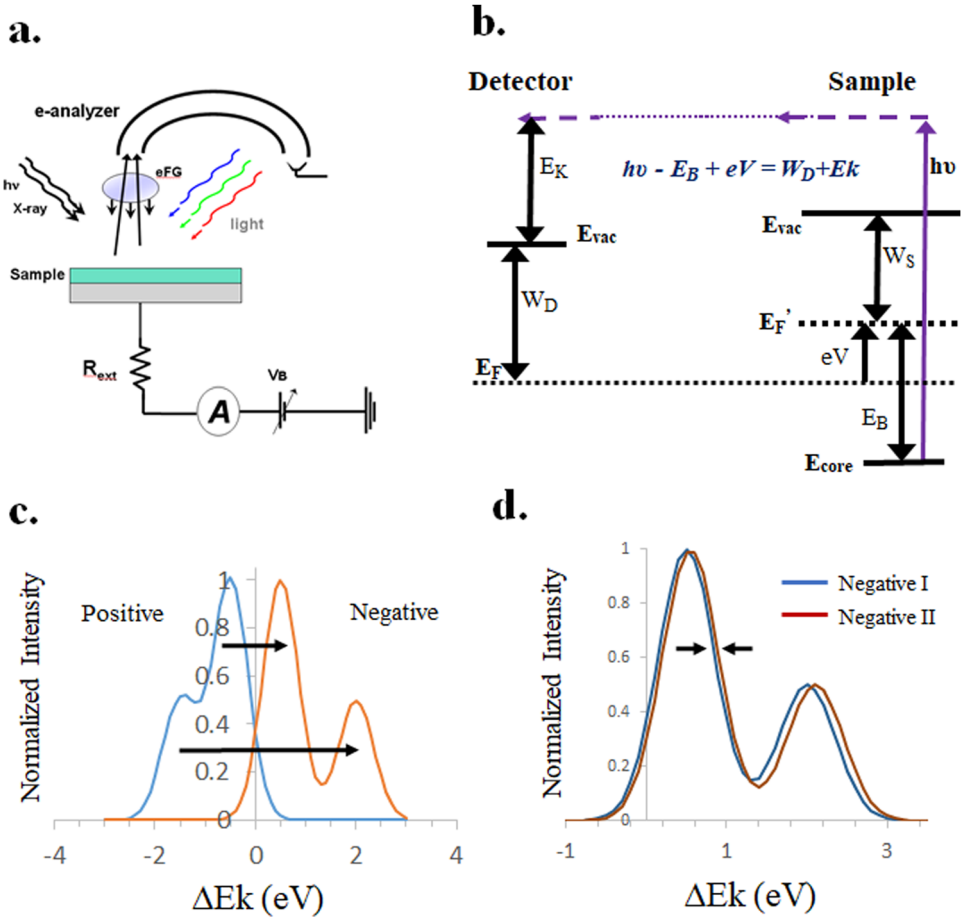

Fig. 1 (a) CREM experimental setup, consisting of four input signals (X-ray irradiation, electron injection from an electron flood gun (eFG), sample biasing (V_B) and light illumination) and two output signals (the photoelectron spectrum at the e-analyzer, exploited as a unique multichannel voltmeter, and the sample current). Different CREM modes make use of these input and output means at different combinations. (b) Scheme presenting the condition for energy conservation, in which the eV term stands for the electrostatic potential at the site of emission, accounting for potentials developed within the sample surface and those supplied externally (note the shift in measured core levels, $E_{core} = E_B - eV$). W_S and W_D stand for the work-function of the sample and the detector, respectively. (c) Simulated spectral splits, exemplifying differential charging (here, the same chemical species in two domains that differ in charging magnitudes). Positive (blue) and negative (orange) charging conditions are shown. The two domain-specific energy shifts upon switching from positive to negative charging conditions are indicated by arrows, demonstrating a way to distinguish chemical shifts from charging artifacts. (d) Simulated energy shifts under slightly varied negative charging conditions. The shift magnitudes are chosen to be much smaller than the line widths and, yet, their derivation can be rather accurate if done at regions of maximal slopes other than peak positions, as indicated by the arrows. The use of kinetic energy (E_k) for the energy scale, other than binding energy (E_B) is preferred because increased electrostatic energy corresponds to increased photoelectron kinetic energy (decreased E_B).

potential component common to many atoms in a given region, similar to the externally dictated potentials in classical electrostatics. Then, the kinetic energy of the photoelectron, E_k, can be written as follows:

$$E_k = h\upsilon - E_B - W_D + eV \quad (1)$$

where $h\upsilon$ is the photon energy, E_B is the 'chemical' binding energy, W_D is the detector work function (a constant to be ignored in the present discussion) and eV is the electrostatic energy associated with the local potential V. Additional terms due to higher order processes may become relevant in specific cases. A scheme representing the energy conservation condition, eqn (1), is shown in Fig. 1b, indicating specifically the measured (E_{core}) and 'correct' (E_B) core levels.

The XPS-based CREM technique enables exploration of this intermixed information and, thus, actively resolves electrostatic from chemical information in the sense mentioned above. Accordingly, the terminology convention on 'surface charging' is generalized to include electricity in its broad context, including dynamic processes and ohmic characteristics.[70] Applied to standard solid-state heterostructures, the differentiation between chemical and electrostatic information has been proven doable and useful, turning the CREM approach to be very attractive for electrical analyses of devices. As an extreme example, pyroelectric specimens such as LTO, STO, or even glycine crystals exhibit reproducible changes in the surface potential under controlled temperature variations, as large as hundreds of volts, for which the CREM approach enables a non-contact means of detection.[71–73] Notably, in biological systems, charge capturing on the atomic scale is a common machinery underlying a variety of bio-processes, *e.g.* in redox centers. Hence, side by side to severe difficulties that are discussed below, great promise is proposed by CREM application to bio-systems, which presents as a whole an exciting field for future developments.

A basic CREM feature, reading electrostatic potentials from XPS line-shifts, is exemplified by Fig. 1c, where an XPS elemental line is schematically drawn on a scale of kinetic energy differences, referenced with respect to the neutral conditions of this element. The simulated line assumes no spin–orbit splitting. Yet, on the left, a split into two overlapping signals is seen, representing positive-charging that gains different amplitudes at two different sample locations. This situation is quite common to XPS: if two surface domains differ in their discharge efficiency to ground, they will develop different charging amplitudes, termed differential charging. Interpretation-wise, the spectrum could mistakenly be thought of as two oxidation states of this element and, based on this spectrum only, it is not easy to distinguish between the two interpretations. However, by charging the sample negatively, as shown on the right-hand side of Fig. 1c, the entire line-shape is modified. First, the energy difference between the two components is reversed in sign and, second, quite common to such experiments, the magnitude of this difference is increased. Such experimental tests of XPS line-shapes are simple and frequently very helpful interpretation-wise, because line-shape modifications can easily distinguish (except for very exotic cases) between electrostatic and chemical non-uniformities. Added to that, Fig. 1d illustrates a typical change in line-shape upon increased negative charging conditions, II > I, demonstrating how the CREM resolving power can exceed by far the bare line-widths; a feature of particular importance in noisy spectra that is based, essentially, on the statistics of the many datapoints in each single spectrum.

Frequently, fine electrostatic information can be extracted by using several elemental XPS lines, exploited as markers that enable the readout of potentials at chemically defined addresses. An example demonstrating this capability is given in Fig. 2. The measured system consisted of a self-assembled

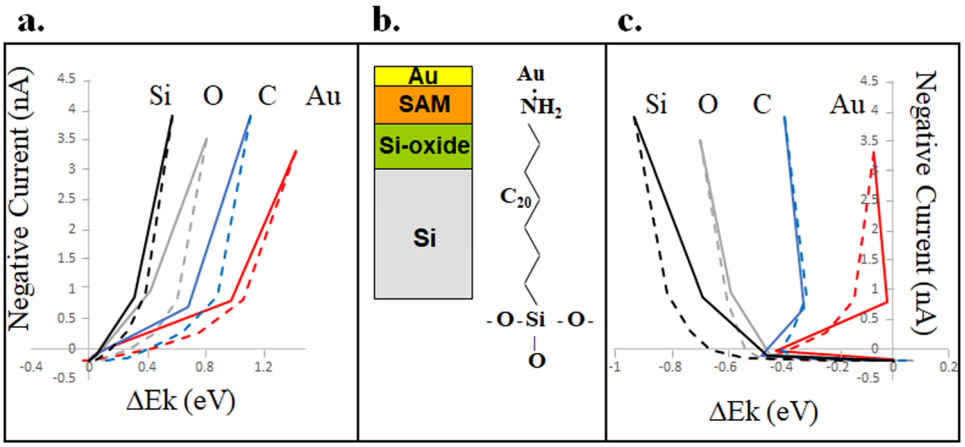

Fig. 2 The non-contact contact: A 'detached' electrode (the eFG) enables direct inspection of potentials underneath. (a) Measured I–V characteristics, already corrected for the sample bias (V_B) changes, where ΔE_k stands for kinetic energy shifts at: the Si-wafer (black), the Si-oxide (grey), the SAM (blue) and the top gold (red). (b) Schematic of the inspected system and its molecular structure. (c) Same as panel a, but with the raw shifts ($\Delta' E_k$), not corrected for the applied V_B. Gradual accumulation of surface charge is best demonstrated by the 'reversed' section in the Au curve, panel (c). Dashed lines stand for the 'way back' in the loop-like scan. Hysteresis is realized in current and potential, therefore appearing very differently in panels (a) and (c). Note the correlation in panel a between vertical ordering (spatially, along the z-axis) and the actual potentials that develop, which provides a rough potential profile for this system. Panel (c) is adapted from ref. 74.

monolayer (SAM) grown on a Si-wafer.[74] Post assembly treatments were used to chemically bind gold to the top groups of the molecules, as illustrated in Fig. 2b. Electrical measurements were performed by operating XPS with the eFG under fixed conditions, while the sample bias, V_B, was varied stepwise. Representative XPS lines were recorded for each of those bias values. The sample current (I), as measured at the back contact of the sample, was recorded as well. The resulting I–V curves, shown in Fig. 2a, present energy shifts (ΔE_k, already corrected for the bias changes). It should be noted that different potentials evolved at different heights of the real-space structure. This is because the top surface is (electrically) an open end, while the back side of the substrate is grounded. It should be a simple exercise in electrostatics to show that each layer potential would float on the potential of the layer underneath, thus forming correlation between the spatial (vertical) and the electrical profiles.[30] Importantly, the substrate in the present example exhibits finite potential changes by itself. However, by directly detecting its signal and evaluating its non-ideality as an ohmic ground, the related potentials can be subtracted, such as to get 'contact free' (recall that no top contact is used) I–V curves, assigned each to a selected domain along the vertical axis. Thus, the electric probe also proposes a fast and simple deconvolution of the information across thin ($\sim$10 nm) layered structures, enabling improved account of the attenuation corrections and hence improved compositional analysis.[39]

Specifically, in the system of Fig. 2, the oxide layer at the interface (see the O 1s curve) develops potential due to its finite impedance. On top of the latter, the SAM (represented by the C 1s line) develops considerable potentials and, finally, the gold atoms provide a probe of the potential at the very top of the structure. Thus, besides the compositional information that can be deduced with respect to the vertical axis, depth profile of the electrostatic potential is also extracted. For example, the difference between C and Au, reflecting the fact that the C-signal integrates over a thickness of $\sim$2.3 nm, should be noted. Due to potential gradients across this layer, its peak position presents an averaged potential readout. A detailed analysis of such averaging features was conducted for and tested with a somewhat thicker Si-oxide layer under varied experimental parameters.[37]

Fig. 2 points to an additional interesting issue. When a top electrode is used in a standard electrical configuration, one can accurately control the applied voltage, but not the actual potential that develops underneath. Frequently, a potential drop emerges at the very interface with the electrode, to which no direct access is enabled. In contrast, CREM enables direct readout of those potentials, as demonstrated by the gold curve in Fig. 2a and c.

The latter point proposes valuable insight into the character of the CREM electrical contact. Qualitatively speaking, it may be considered as a kind of soft electrical contact, with no 'real' solid-state interactions and, in turn, with a unique access to its effective interface. Fig. 2c exemplifies this capability by presenting the raw line-shift data, Δ'Ek, similar to Fig. 2a, but prior to applying corrections for sample bias changes. For sufficiently negative bias voltages, the eFG electrons are fully repelled and therefore the sample builds up positive surface charge, induced by the X-ray source. However, as soon as the negative bias is sufficiently lowered for allowing some eFG electrons (those of highest energy) to land on the surface, negative charge starts to accumulate. The bias value at this inflection point is termed IP.

Interestingly, the four elemental curves in Fig. 2c present two qualitatively different shapes. As manifested by all the curves, when the sample's negative bias is decreased and, thus, allows an increase in the flux of incoming electrons (hence, increased sample current), the XPS lines undergo only partial shifts, smaller than those dictated by the bias. This difference is due to the evolution of surface fields. For O and Si in Fig. 2c, the curves exhibit a monotonic behavior. However, the curves of C and mainly Au manifest an unusual response in which, for a given step in sample bias, the raw line-shift takes a sign opposite to the one dictated by the bias. This 'turning-back' feature reflects the actual accumulation of electrons at surface states, offering a unique view of the semi-contact behavior. For each step, the amount of negative charge is stabilized upon reaching a dynamic balance between the flux-in and flux-through samples. This steady-state is self-tuned: the surface potential acts as a barrier against incoming electrons and, when varied due to charge accumulation, the barrier height varies too, such as to finely adjust the flux-in. Namely, an increased flux of electrons would gradually build up its own barrier. Frequently, it is possible to follow in real time (on scales of seconds to minutes) the gradual formation of this balance (not shown here due to the evolution of SAM damage, see below).

Similar to the example in Fig. 2, where local potentials could be extracted for different layers, organic molecules frequently propose atomic addresses that can, in principle, provide atomic-resolution of the electrical data. An example of such CREM capabilities may be found in Fig. 3 and related publications.[40–42] The figure shows results from SAMs of small molecules, for which the potential profile is non-linear, or even non-monotonic, revealing a couple of interesting features. First, clear differences between atomic-scale sites are manifested in Fig. 3a on a sub-nm scale, evaluated under conditions of excellent reversibility, namely, prior to damage evolution (see discussion below). Notably, signal is collected over laterally macroscopic scales and, yet, the atomic scale variations are resolvable, indicating that lateral homogeneity over the inspected SAM is sufficiently high to avoid smearing of the intra-molecular details. Second, the molecule–substrate interface potential is resolved (compare the data points of Si and In, the latter standing for the ITO substrate), such that molecule-specific information can be extracted (note in particular the difference in the interfacial potential drop of the two samples in Fig. 3a). Third, though at limited accuracy, molecular polarizability is revealed and quantitatively evaluated by the CREM probe.

Calculated curves are shown in the figure, using density functional theory (DFT) for gas molecules under an artificially

a.

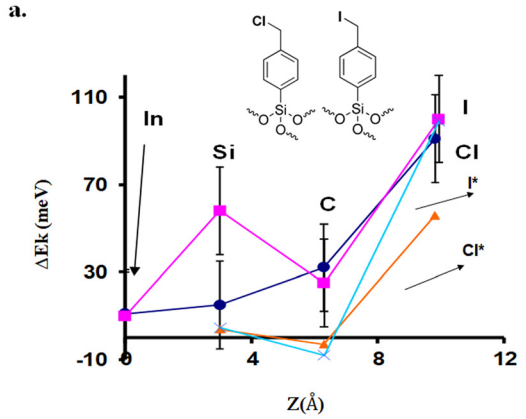

b.

	Si	C	Cl	I	H
Covalent radii (A°)	1.11	0.67	0.79	1.15	0.53

Fig. 3 Atomic scale CREM. (a) Intra-molecular potential profiles obtained under low flux of eFG electrons, showing experimental data for I- and Cl-terminated (violet and blue, respectively) SAMs on ITO, together with corresponding DFT-based calculations, marked by * (light blue and red, respectively). The inset schematically depicts the molecular structure. (b) Values of covalent radii used for the calculated potentials. Note the non-monotonic potential profile obtained for the I-terminated molecular layer, revealing a strong polarizability response at the phenyl ring upon electron density increase around the iodine site. Experimental data in panel (a) were taken from ref. 40.

applied external field. Covalent radii taken from the literature are given in Fig. 3b. Supported by the calculations, the experiments show that, in response to charge density increase at the halogen top site, the phenyl ring polarizability acts to locally deplete the electron density while the Si atom gains enhanced electron density. Consequently, sensitivity to details in the molecular polarizability is demonstrated. A difference in the magnitude of this effect is noted for molecules with a different halogen termination, I *vs.* Cl, and also (not shown here) for varied molecular backbones.[41]

The above couple of examples demonstrate the added value of having chemical addresses for the readout probe. Needless to say, the capability to directly measure fine electric information across sub-molecule scales is extremely challenging for any of the existing electrical probes. Another unique aspect of the CREM technique is associated with its power supply. As already mentioned, in contrast to standard electrical tools, charge is supplied from a filament that serves as a distant source of electrons, the eFG. These are hot electrons, landing on the sample at energies (slightly) above the vacuum level, which is fundamentally different from standard techniques where electrons are injected around the Fermi level, supplied from an electrode that is physically connected.[39] Similarly in this respect, hot positive charge is created by the X-ray irradiation *via* emission of electrons to the vacuum. The latter is not fully analogous to the eFG operation as it bears a limited dynamic range, with nearly no control on energies and a poorly defined location of the charge generation.[75] Yet, in this case too, the resulting holes are hot. Thus, CREM is operated under conditions that are fundamentally different from those in standard techniques, bearing hot charge characteristics at the basics of the technique.

In some cases, the latter point presents an important advantage over standard tools.[39] However, when contact-like characteristics are of research interest, it is important to account for the hot-charge issue in the interpretation of results. Typically, the hot electrons attenuate and thermalize along several tens of nanometers. Therefore, for very thick samples, the *I–V* characteristics become identical to those of standard techniques. However, for thin layers, which is usually the limit of interest in XPS studies, the *I–V* characteristics are necessarily different, because some of the injected electrons can cross the layer without even interacting. This issue is expressed by the following simple model for *I–V* characteristics at the limit of infinitesimally thin layers.

3.2. CREM *I–V* modelling

Consider a thin dielectric layer with a single type of electron trap at surface density N. The layer is exposed to an incoming flux, I_0, of eFG electrons, for which the trapping efficiency, A, is constant. The substrate is assumed to be a perfect metal, and the discharging efficiency from traps to ground, B, is assumed to be constant too. The total amount of captured charge per unit area, Q, is given as follows:

$$Q = Nef$$

where e is the electron charge and $f \leq 1$ is the partial occupation function.

The rate equation for trap occupation can be written as follows:

$$\dot{f} = A(1 - f) - Bf \quad (2)$$

In the limit where $f(t = 0) = 0$, the solution takes the following form:

$$f(t) = A\tau(1 - e^{-t/\tau}) \quad (3a)$$

where

$$\tau = (A + B)^{-1} \quad (3b)$$

Experimentally, the time evolution $f(t)$ can be limitedly followed, subjected to the detection rate in XPS. Time-dependent CREM studies[76,77] show indeed, in agreement with eqn (3), an exponential build-up of the potential, frequently with time constants in the ms to sub-second regime. Much larger time constants have been reported as well.[70,78] The charging and discharging processes in the present case bear aspects similar to those of regular *RC* circuits. However, it should be stressed that associating the CREM time constants with the classical resistance (R) and capacitance (C), as proposed in related experiments,[79,80] would be misleading, because hot charges, far above the Fermi energy, E_F, are involved here.[39]

Upon signal detection rates that are much slower than τ, one effectively records the steady-state limit, at which the trap filling function, f, approaches:

$$f(\infty) = \frac{A}{A+B} \tag{4}$$

As intuitively expected, the latter formula expresses the competition between capturing and discharging rates. The I–V characteristics may now be derived under the following approximations:

(1) The capturing constant, A, is assumed to be proportional to the incoming flux of electrons (I_{in}), and to possibly include an energy dependent term, $a(E)$: $A = I_{in}a(E)$;

(2) The discharging constant, B, is assumed to be independent of the incoming current, *i.e.* fully dictated by the sample itself. Its energy dependence may be expressed by a function $b(E_T)$, where E_T is the trap energy level: $B = b(E_T)$.

As already mentioned, both A and B are assumed to be time independent and, in particular, bear no dependence on the filling factor f.

As the surface potential correlates directly with the filling factor, it may be expressed as follows:

$$V = V_m(N,Z)f$$

where V_m is the maximal potential magnitude, achieved under full occupation of the traps. It depends on the 2D trap density, N. Possibly, V_m may also depend on a geometrical function, Z, relevant to thicker structures (*i.e.*, beyond the present model) where the location of traps with respect to the substrate does matter.

At the steady state, the current measured on the sample back contact is equal to the incoming current, $I_{in} = I_{sample} = I$. It is possible then to use the above equations and express the I–V characteristics as follows:

$$I = \frac{b}{a}\frac{V/V_m}{(1 - V/V_m)} \tag{5}$$

where, for convenience, the dependence of a, b and V_m on energy and/or system parameters is omitted.

At its low-V limit (small f values), the I–V function is linear. For high-V values, one encounters saturation characteristics, corresponding to full occupation of the traps. This limit of saturation presents an important difference from the classical case of RC circuitry. Even if the physical mechanism of trap filling is similar, the current can increase continuously in CREM (see reservations below) and eventually diverge for $f = 1$, because injected electrons are free to cross the layer and be collected at the bottom contact. In contrast, the current magnitude in a classical RC circuit would approach a minimum when the voltage approaches saturation.

The model is phenomenological and, usually, its parameters cannot be determined rigorously. In turn, it presents a convenient template for quantitative evaluation of processes in systems that are not fully defined. Not accounted for by this simple model, complications of various types may be needed to be addressed in practical analyses, including the finite thickness of inspected layers, diversity of traps and charge carriers; features that are partially treated by models discussed below. Yet, a particularly important parameter that is not dealt below should be noted. It regards the dependence of charge injection efficiency on the surface potential, which turns the problem into a non-linear one. As soon as $a(E)$ is energy dependent, any build-up of surface potential will affect the kinetic (the landing) energy of eFG electrons and, hence, affect the trapping efficiency, $a(E)$. In particular, close to zero kinetic energies, this non-linearity can lead to pronounced effects of a near-resonance character (to be discussed elsewhere).

3.3. Comparison to other techniques

With a risk of over simplification, it may be useful to present a concise comparison between CREM and other techniques. Given the interdisciplinary nature of CREM as a bridge between XPS and electrical probes, two technique families may be distinguished for such a comparison: (1) XPS-based methods and (2) the various electrical measurement techniques. Both technique families involve a plurality of variations and approaches. Therefore, a limited selection is used hereafter, such as to emphasize the features of significance in the context of CREM.

With respect to XPS-variants, CREM can, in principle, be combined with most of them, including cryo-XPS and near-ambient pressure (NAP) XPS. Practically, some CREM features may become more challenging under specific experimental restrictions; however, the electric information can still be harvested. Table 1 summarizes the key issues of concern in such modes.

Compared to the ***XPS-based techniques***, CREM provides the following valuable features:

a. Access to a broad range of electric characteristics
b. Enhanced sensitivity to defects
c. Enhanced sensitivity to X-ray-induced damage
d. Improved chemical analysis *via*:
   i. Improved line-shapes
   ii. Improved determination of oxidation states
   iii. Improved attenuation correction factors for each specific signal
e. Indirect access to hydrogen contents

Main disadvantages of the CREM application are:

a. It is a slow technique (due to the multiple scans over selected spectral windows)
b. Enhanced beam-induced damage frequently appears under elevated fields

Comparison to ***standard electrical measurement techniques*** is given in Table 2. It presents selected standard commercial instruments, whereas much expanded capabilities and resolution can be found with state-of-the-art types. To some extent, these techniques too may be combined with CREM, because CREM can be employed using direct contacts to the sample.[81–83] However, contact-CREM configurations were not tried yet in our laboratory and, therefore, are not referred to in Table 2.

Table 1 Motivations and concerns in operating CREM under various non-standard yet well-established XPS modes: (1) low-temperature (cryo); (2) near-ambient pressure (NAP); (3) angle-dependent (ARXPS); (4) ion-beam sputtering; and (5) high-energy (hard) X-ray sources (HAXPES)

Mode	Motivation	Concerns
Cryo	Improved sample stability Suppressed dehydration	Electric properties may vary significantly. Condensation of gas molecules can occur. The double-side carbon tape resistivity tends to increase at low temperature. Systematic noise (in the Kratos design) introduced upon simultaneous use of the back-contact current detection and the thermocouple.
NAP	Suitable for wet (and other high vapor-pressure) samples	Decreased CREM dynamic-range. Reduced signal intensities. Appearance of foreign (gas molecules) signals
ARXPS	Independent depth profiling	Sample's tilt affects the effective eFG flux. It also affects the X-ray induced charging.
Sputtering	Depth profiling down to deep regions	Drastic changes in the electric properties (even upon very gentle steps and even with Ar-clusters).
HAXPES	Probing deeper regimes. Getting access to additional core levels. (Synchrotron facilities enable various additional options).	If operated under elevated beam power (due to decreased signal intensities), difficulties emerge with sample stability; also in light-induced CREM.

Reliability as well as a deep understanding of CREM technique fundamentals was mostly developed with well-behaved inorganic samples, not described here.[39] Consistency between the electrical data and the *in situ* standard XPS results was tested and confirmed. In particular, strict correlation was demonstrated between the line-shift due to vertical fields and the depth-dependent signal intensities. The latter was demonstrated by specially prepared sets of layered samples,[30] as well as by varying the sample tilt angle.[34] More challenging in this respect are those surfaces presenting lateral heterogeneities.[31] Similarly, systematic studies were conducted on sample temperature dependencies in polar materials,[30,73] photovoltaics at semiconducting systems,[36,38] and more.

Consistency with independent characterization techniques was already tested in various CREM-containing multi-technique studies.[93–95] The latter included infra-red (IR) spectroscopy, photoluminescence (PL), electron paramagnetic resonance (EPR), nuclear magnetic resonance (NMR), X-ray diffraction (XRD), and electron microscopy (EM) techniques including electron energy loss spectroscopy in transmission electron microscopy (TEM-EELS), atomic force microscopy (AFM), contact angle (CA) measurements and more, which are tested on a variety of specimen types.

Of particular importance, attempts for direct comparison to standard electrical measurements were conducted, using well-behaved systems. Part of those tests were published.[39,96] While showing perfect consistency in potential readouts, fundamental differences could also be identified, due to the fact that hot charges are activated and take part in those conduction processes probed by CREM. Thus, fundamental differences emerge: (1) unique features frequently show up in the CREM data; and (2) quantitative comparisons with standard electrical data may be more involved and, possibly, not as direct and simple.

As already stated, organic systems frequently present severe issues of sample stability and, consequently, non-trivial issues of measurement reliability under X-ray irradiation and elevated electric fields. To address this difficulty, our experimental protocols include routinely: (1) fast early scans; (2) a learning stage of the damage evolution, usually on one fixed point; (3) using different fresh points to confirm the validity of results; and (4) repeating measurements on fresh samples.[70] Importantly, response reversibility is always checked. Any input signal (for example, switching the eFG on) is followed by a back step (switching off) in order to verify reversibility in line-shifts and sample current. Hysteresis is frequently encountered, which may make these checks more involved. Cases of insufficient reversibility (as compared to the measured reversible component) are classified accordingly and are subject to exclusion from the log of 'pure electrical' data.

4. Beam-induced damage studies

4.1. Probing damage by CREM

Back to the early 90's, XPS was considered a non-damaging technique, mainly in reference to another surface analytical technique, Auger electron spectroscopy (AES), where an electron beam was used. However, organic molecules are known to be sensitive to ionizing irradiation, hence the appearance of damage processes under the XPS probe is not surprising. In an early work on this issue,[97] XPS of various alkane chain-based self-assembled molecular layers (SAMs) was used in combination with *ex situ* IR spectroscopy, such as to cross-check the XPS-evaluated damage. It was shown indeed that XPS is insensitive to a major part of the damage processes and, in particular, to protonation processes and H evaporation. With thick polymers it was quite difficult to even notice any damage progression, but with nanometrically thin layers, effects could be partially followed by the XPS too.

This comparative study, XPS and IR spectroscopy, further demonstrated the critical role of kinetics in damage evolution. By introducing highly X-ray sensitive groups to the SAM, COOH or COO^-, for which XPS is an excellent quantification probe, it was possible to dictate a specific initiation of the damage processes and, thus, affect the degradation evolution, rate

Table 2 Comparison of CREM with common electrical measurement techniques: impedance spectroscopies – standard (contact, IS) and electrochemical (EIS); probe techniques – Kelvin probe force microscopy (KPFM) and conductive AFM (c-AFM)

	CREM	IS[84,85]	EIS[85,86]	KPFM[87,88]	c-AFM[89]
Measured quantity	Element-specific electrical response	Frequency-dependent complex impedance	Complex impedance (magnitude and phase) over frequency	Contact potential difference (CPD)	Local current response under bias
System configuration	XPS-based setup under controlled electrical stimulation	Electrode-based system, often 2-terminal; applied to passive materials or non-faradaic systems	Two- or three-electrode setup; macro or microelectrodes	Non-contact AFM mode with dual-pass scanning (lift mode)	Contact mode AFM with conductive tip
Top contact type	Non-contact (eFG and spectrometer replace physical electrodes)	Physical contact *via* electrodes on sample surfaces	No direct contact; electrical contact *via* electrolyte	Non-contact (lift height ∼ 10–100 nm)	Physical tip-sample contact
Environment	Ultra-high vacuum; Dry	Dry, humid, or physiological environments	Ambient, hydrated, or fully immersed systems	Ambient, vacuum, or humidified chamber	Ambient or dry; limited liquid compatibility
Availability of chemical information	High – directly linked to chemical identity *via* photoelectron spectra	Low; not chemically specific	Low; not chemically specific	Low to moderate – indirect correlation with chemical states	Low
Lateral resolution	Poor; 10–100 μm, but can reach atomic site specificity	None; or ∼μm-scale if patterned electrodes used	None or ∼μm scale with microelectrodes	High (atomic[90–92] to 50 nm) – tip and height dependent	High (∼10 nm) – tip contact area dependent
Depth resolution	Very high, down to ∼0.2 nm, depending on the inspected dielectric properties	No direct depth discrimination; inferred *via* circuit modeling if layers exhibit distinct time constants	None directly; inferred *via* circuit modeling if layers exhibit distinct time constants	None directly. < 5 nm effective – surface-sensitive (subsurface polarization contributes)	Indirectly ∼1–10 nm – based on tip-sample contact volume and mechanics
Frequency range	Quasi-static up to slow (kHz) modulations	Broad: typically mHz to MHz	Broad: mHz to MHz	Static or AC modulation (∼kHz)	DC to low-frequency *I–V* sweeps
Key advantages	Resolving inner domains. Hot-e sensitivity. Direct link to chemistry. No top contact.	Simple, robust, non-destructive.	Probes both bulk and interfaces. Suitable for *in situ* analysis.	High surface sensitivity. Work function mapping.	High-resolution electrical mapping. Defect localization.
Limitations	Requires UHV and XPS access. Complex interpretation	Contact-formation issues; bulk averaging; no chemical specificity; requires models for interpretation.	No lateral resolution. Dependent on model fitting.	Sensitive to contamination; requires clean, flat surfaces.	Tip wear. Sample damage in soft materials.

and final products. Two extreme cases were thus examined. The first, with COO^- as binding groups to the substrate, was found to involve increased evaporation of the entire molecular backbone, to be distinguished from the 'usual' evaporation of small molecular fragments. In the second case, SAMs consisting of alkanes with top COOH groups were used, such that initiation of the radiation damage was restricted to the top surface. Cross-links were then rapidly formed between neighboring top sites, which turned them into an effective blocking barrier against hydrogen evaporation. Thus, in contrast to the first case, monolayer degradation was suppressed considerably and a much higher SAM robustness was achieved.

Interestingly, while inherently XPS is insensitive to H-related damage, CREM proposes *in situ* enhanced sensitivity to such processes, allowing their improved characterization and evaluation. It is well known that electrical properties are likely to be very sensitive to defect states. Therefore, breaking C–H bonds would likely affect the SAM electrical properties and, thus, be sensed by CREM. Fig. 4a presents a test experiment, dedicated to the CREM evaluation of beam-induced damage in a high-quality SAM of alkane chains on a Si substrate.[74] Several rapid CREM-derived *I–V* loops are shown, performed on the C 1s line first, then on the Si 2p line and back on the C 1s line. In accordance with the model description in Section 3b, the *I–V* curve governs (1) current readouts at the back contact of the sample, and (2) line-shifts extracted from XP spectra of selected elements, as measured under controlled changes in eFG parameters. Remarkably, as demonstrated by the first and last carbon *I–V* curves, C(I) and C(II), respectively, during a period of $\sim$3 minutes of very gentle exposures, the sample current increased by a factor of $\sim$2.5. As a reference, for the same irradiation time, no XPS or IR signs of damage could be found. The electrical result is explained by the formation of defects within the layer, as illustrated in the lower inset of panel a. Electrons supplied from the eFG and captured at the top surface could thus traverse the layer, down to the substrate, *via* short 'jumps' instead of the pure (long path) tunneling.

In order to check this issue quantitatively, a simple model was employed, based on rate equations in a 1D description of the transport process, solved for the steady-state case. A scheme of the model system is given in Fig. 4c, where gap-states represent the defects, with an energy that lies between the valence and conduction bands. Subject to minor simplifying assumptions, an analytic expression was derived for the *I–V* curve and, specifically, to its dependence on the number of defect states, *N*, along the (1D) transport path across the insulating medium. The details of the derivation are given in the Supplementary Information of the original paper, yielding a rather simple final expression:

$$I \sim \frac{VC}{\sum_N} \exp\left[\frac{(V - B - b)D}{N + 1}\right] \quad (6)$$

where *C* is the capacitance of the layer, *D* is its thickness, and the energy parameters, *B* and *b*, are barrier heights of the inherent surface states and the newly formed (inner) defect states, respectively. *B* and *b* were varied (not shown) such as to cover a reasonable range of the SAM properties. The symbol at the denominator is defined as follows:

$$\sum_n \equiv \sum_{j=0}^{n} \beta^j$$

where the β^j parameters express the ratio between forward and backward tunneling probabilities from a given defect, *j*, to its (down-stream/upstream) neighboring defects.

Fig. 4b presents *I–V* curves calculated for specific *N* values with a selected set of parameters. As intuitively expected, the ideal exponential *I–V* shape of tunneling across a perfect insulator, namely the $N = 0$ case, gradually transforms into an ohmic (linear) *I–V* shape for large *N* values; a limit already approached with these model parameters for $N \approx 5$.

Experimentally, the net potential drop across the SAM itself, namely with the substrate's potential being subtracted, was obtained by referring the shifts of the C 1s line to those shifts extracted from the O 1s line (corresponding to the potential changes of the thin oxide at the Si-monolayer interface). The experiment was performed under sample cooling to 150 K, such that damage progression was slowed down. Cooling is a common means for effective suppression of beam-induced damage, already demonstrated by various cryo-XPS works,[52,98] cryo electron microscopy[10,11] and more. Cryo-CREM tends to introduce technical difficulties, such as changes in the conductivity of the adhesive carbon tape and/or the substrate. Specifically, at the Weizmann laboratory, the temperature control setup employs electric pulses that can distort the recorded spectra. These difficulties are all addressable; however, their detailed discussion is not attempted here.

As shown in the top inset to Fig. 4a, a nearly exponential *I–V* shape was indeed obtained during the early stages of the experiment (see the straight line in log-scale, Fig. 4a, yet with a slight deviation from linearity already noticed at the limit of high currents). Fig. 4d presents the model-predicted dependence on the number of defects, *N*, calculated for four different combinations of parameters. Experimentally, as shown in Fig. 4e, a smooth, gradual rise is observed for the sample current over long time scales, eventually approaching saturation. This behavior is due to the 3D distribution of defects, which is not accounted for by the 1D model.

It should be noted that among various SAMs that were inspected in our laboratory, it was quite rare to obtain such an exponential *I–V* curve, even for very early stages of exposure to the X-ray, which indicates on the quality of the as-received SAMs in this case, being practically 'free' of defects. Altogether, these experiments demonstrate remarkable electrical sensitivity to both the intrinsic defects and the emerging damage, far better than the sensitivity of IR or standard XPS spectroscopy. CREM is conducted *in situ* to the XPS, with no need for a top contact and, by exploiting elemental addresses, the role of substrate's impedance can be easily eliminated, which is a critical feature for properly testing the exponential *I–V* functionality. Thus, a probe that is essentially blind to hydrogen

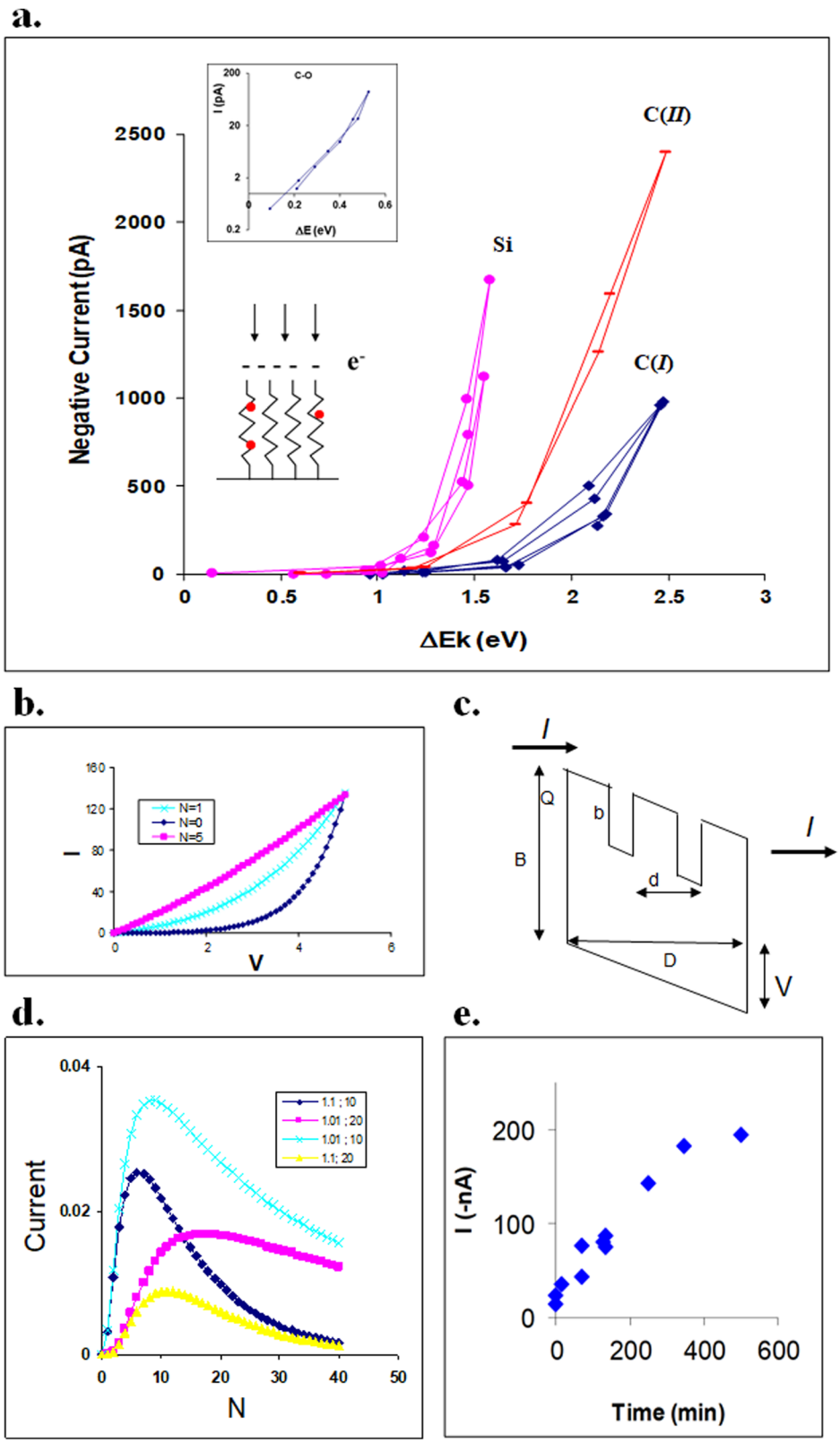

Fig. 4 Electrical evaluation of damage. (a) Rapid *I*–*V* curves of a molecular monolayer, performed at *T* = 150 K: two C 1s loops recorded first, C(I), followed by two Si 2p loops, Si, and again a single C 1s loop, C(II). Note the consistent increase in sample current. The insets show the log-scale 'C minus O' *I*–*V* curve (top) and an illustration of damage formation in the SAM (bottom). (b) Model calculated *I*–*V* curves for selected values of the number of defects (N) with an arbitrary choice of barrier parameters (*b* and *B*) and capacitance (*C*). The current is normalized to a common scale, showing the transformation from a roughly exponential to a roughly linear shape. (c) Schematic presentation of the model structure, indicating the two barrier height values, *B* and *b*, and barrier widths, *d* and *D*. (d) Simulated dependencies of the current magnitude on *N*, calculated for two values of *β*, 1.1 and 1.01, and two values of the effective barrier parameter, (*B* + *b*) *D* = 10 and 20. (e) Experimentally documented current magnitudes along extended time scales. Adapted from ref. 74.

turns into a tool of superior sensitivity to hydrogen-related processes and evaporation in particular.

4.2. Desorption of halogen atoms

Similar in a way to hydrogen bond breaking and evaporation, the tendency of halogen atoms to escape from the surface is a well-acknowledged sample degradation process, frequently referred to as a maintenance problem in UHV instruments. Besides thermal energy that enables spontaneous desorption, the X-ray photons can probably stimulate the evaporation *via* core-electron excitations and ionization processes that shake the electronic configuration abruptly. Moreover, the application of eFG was found in some cases to accelerate the halogen desorption by 2–3 orders of magnitudes, in particular with SAMs of halogen-terminated alkane chains (unpublished data). In contrast, eFG application can be totally insignificant with respect to damage formation in other molecular layers. Hence, predicting the magnitude of these effects is not necessarily trivial. Fortunately, in contrast to hydrogen evaporation, quantitative evaluation of the halogen amount can be obtained by directly monitoring its XPS signals.

An interesting result in this context is shown in Fig. 5. The studied system consisted of iodine- or chlorine-terminated molecules, self-assembled on ITO, as shown in Fig. 5c.[40] As a function of irradiation time, the total amount of iodine gradually decreased, accompanied by a gradual change in the shape of the I 3d line. Apparently, the time dependence of iodine amount, expressed in Fig. 5a as the I/Si atomic ratio for both measurements without and with the eFG, did not obey a simple statistical dependence, but a log(t) functionality. To be distinguished, a similar sample with Cl-terminated molecules did not follow this unusual time dependence, except for its very early stages of exposure to irradiation.

The time dependence of iodine intensity ($I(t)$) can be expressed phenomenologically as follows:

$$I(t) = I_0 - B\cdot\ln(1 + t/t_0); \quad t > 0 \tag{7}$$

which resembles aging processes.[99] It yields for the rate of material loss:

$$-\mathrm{d}I/\mathrm{d}t = B/\{t_0(1 + t/t_0)\} = B/t_0\cdot e^{-I0/B}\cdot e^{I/B}$$

Namely, an exponential dependence:

$$\mathrm{d}I/\mathrm{d}t \sim -\exp(I/B) \tag{8}$$

Such a behavior is very different from the trivial relationship, $\mathrm{d}I/\mathrm{d}t \sim -I$, typical to non-interacting neighboring sites. The exponential dependence found here, eqn (8), reflects inter-iodine interactions, believed to effectively express in-layer stress upon dense assembly. Such a formation of stress is typical to systems in which the energy gained upon binding to the substrate is comparable and opposite in sign to the energetics imposed by interactions between the adsorbed species. In the present case, binding *via* silane groups to the substrate competes with the steric constraints introduced by the large size of the iodine atom. The latter density conflict was, apparently,

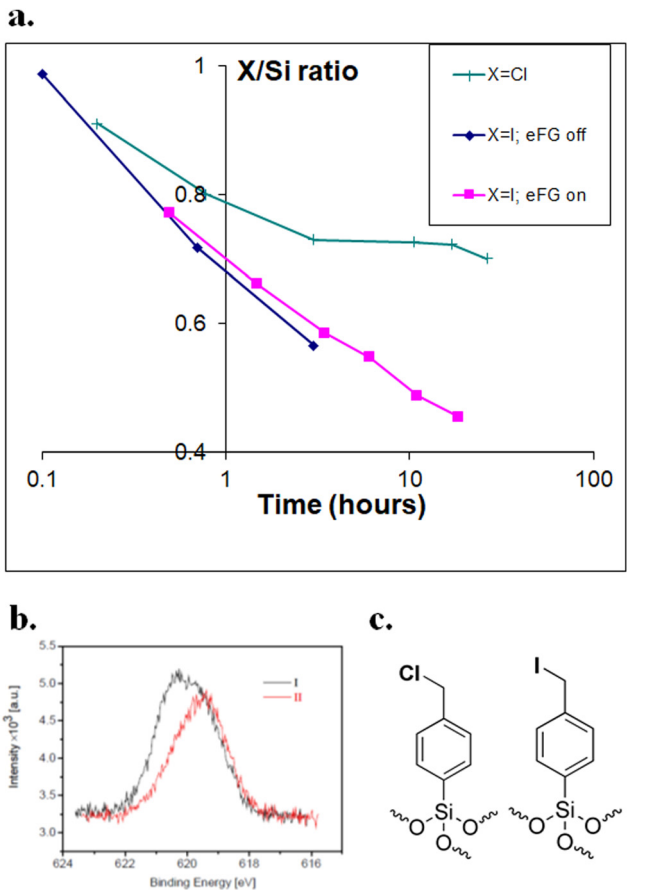

Fig. 5 Halogen desorption from molecular layers. (a) Halogen amount, normalized to the amount of Si, as a function of irradiation time, given on a log(t) scale for both I- and Cl-terminated SAMs. (b) The I 3d line recorded at different times of the experiment, I and II, demonstrating pronounced line-shape changes. (c) Molecules used for self-assembly on ITO. Taken from ref. 40.

much more pronounced for iodine than for the case of chlorine termination (see the time dependence of Cl-terminated SAMs, Fig. 5a). The two competing density optima would therefore give rise to incommensurate assembly[100,101] that relaxes stress by developing structural defects, or even a super structure. For example, self-arranging in two or more alternating states, or alternatively, breaking the assembly continuity over a characteristic domain size, is a well-documented phenomenon. Then, back to the present system, any beam-induced evaporation of an iodine atom would assist the release of stress in a corresponding domain. As directly quantified by the XPS atomic ratios, the latter can be distinguished experimentally from the process of desorption of an entire molecule, or the intrinsic existence of assembly vacancies.

The 'fresh' I 3d line-shape, shown in Fig. 5b, exhibits indeed a split attributed to two or more different states that coexisted in the dense phase of the layer. Degradation in this experiment involved a gradual change in line-shape, indicating that the 'less reduced' iodine states suffered much faster intensity decrease. Further research is needed here in order to distinguish between desorption events that might be restricted from

the first place to weaker bonds in an alternating superstructure (those of lower electron density) and, alternatively, stress relaxation within domains of a gradually diminishing size. This way or another, the drive for iodine evaporation involved here pronounced collective effects.

A potential lesson is proposed by this study. Beam damage suppression is usually motivated by the attempt to collect data from the bare, unperturbed surface. Even if closely approached, this goal is in principle non-realistic, because during the very early stages of an experiment, the sample already accumulates some history of exposure to radiation and, if the impact is highly non-linear, it will be difficult to estimate its magnitude. Moreover, storage history in a vacuum chamber and, possibly, issues like the proximity of the analysis spot to an adhesive tape should all be considered. However, by inspecting the damage processes and their evolution, one can greatly assist the analysis. First, following the evolution of damage with time, as done here, the extrapolation to zero exposure can be improved and, accordingly, the XPS quantification may be corrected. Second, damage processes can potentially teach on sample's characteristics that the standard XPS analysis cannot access; sometimes even solve XPS interpretation pitfalls. With iodine-terminated molecules it was the in-layer stress that could be learnt on. A plurality of additional features, starting from spatial organization information and ending in bond strength and stability issues, may potentially be discovered once this approach is adopted. Third, an additional important category of the potential hidden in damage studies regards the use of damage as a 'writing' means; namely, controlling and utilizing the irreversible modifications in samples in order to obtain a desired feature. In the following, a few examples of promising works in this direction are described.

4.3. Beam-induced transformations as a writing means

Damage processes such as the one demonstrated in Fig. 4 present a useful feature that may be straightforwardly exploited as a writing process, because an insulating layer was undergoing improved conductivity in this example. In a following work, beam-induced hydrogen evaporation from SAMs of alkane chains was shown to result in a leading process of C=C double-bond formation within the SAM.[102,103] Improved electrical conductivity was thus established and, therefore, irradiation could be used as an effective 'doping-like' process, in analogy to doped semiconductors. In practice, relatively high concentrations of defects, of the order of 3%, were needed in this case for obtaining sufficient contrast in conductivity. However, the potential opportunity of using focused, high-energy beams, *e.g.* collimated X-rays or even electron beams, to write circuits on planar SAMs could be considered.

An exciting demonstration of advanced X-ray-induced chemistry was accomplished by Sagiv and Maoz *et al.*,[94] as part of a project initiated as 'constructive lithography'.[104] Oxidation reagents from a sacrificial PVA layer, 4–6 nm thick, were directed to its interface with a high-quality OTS monolayer, as shown in Fig. 6a, where they selectively transformed the CH_3 end-groups of OTS into COOH. The process was activated by the X-ray beam of the XPS spectrometer, but as a proof of concept, additional activation means and chemical processes were demonstrated (see the original paper). After irradiation, the irradiated PVA layer could be *ex situ* removed by a scotch-tape, exposing neatly the underneath OTSox monolayer for additional characterization and reactions. As shown in Fig. 6b, FTIR quantitatively evaluated the transformation of CH_3 into COOH groups, indicating (within the FTIR sensitivity) full completion of the chemical transformation. Complementarily, as shown in Fig. 6c, XPS revealed that the resulting OTSox layer presented accurately the theoretical atomic ratios and chemical shifts. Additional chemical processes were developed in related works by Sagiv, such as to extend the 'writing' action by multiple steps on nanoscale areas. Writing means much finer than the poorly focused X-ray beam were shown to retain high quality and thus enable improved line widths, of the order of 20 nm.[105]

As a partial summary, the damage-related studies point to a two-fold challenge in the XPS of soft matter: first, damage is likely to be a considerable side-effect and, second, the probe itself is not quite sensitive to have all these degradation effects being noted. Therefore, great caution should be taken in the interpretation of results and, highly recommended, in the experimental protocols adopted for biomaterials. In particular, the limited resolving power of XPS encounters the very heart of conformational and fine C–C and C–H bond variations that underlay diversity in biological structures and functions. Electrical information obtained *in situ* by CREM can become remarkably helpful in these cases. In the following, a dedicated CREM mode that focuses on samples' response to light illumination is demonstrated, presenting a novel characterization mode, as dealt in the next two sections.

5. Light-induced charge transport across dithiol monolayers

5.1. Competing transport mechanisms

Aspects of the mutual dependencies between structure and electrical properties in assemblies of organic molecules may be demonstrated by the following study of charge transport characteristics across self-assembled molecular layers (SAMs).[106] The system consisted of (1) top CdSe nanoparticles (NPs) that functioned as light absorbers, (2) a gold substrate that served as the charge collector and (3) a spacer between the two, for which dithiols with different backbones were used, as shown in Fig. 7a. Under LED illumination at 630 nm, electron–hole (e–h) pairs could be generated selectively at the CdSe NPs, thus achieving a well-defined source for the charge transport processes. XPS line shifts were measured to extract the photovoltage (PV) developing locally at the NPs due to charge transfer to the gold. Complementarily, photoluminescence (PL) due to e–h recombination within the NPs was *ex situ* measured, indicative of those charges that were not transported to the gold.

Recalling that self-assembly on gold is relatively well controlled, the system seemed to be rather simple for a detailed

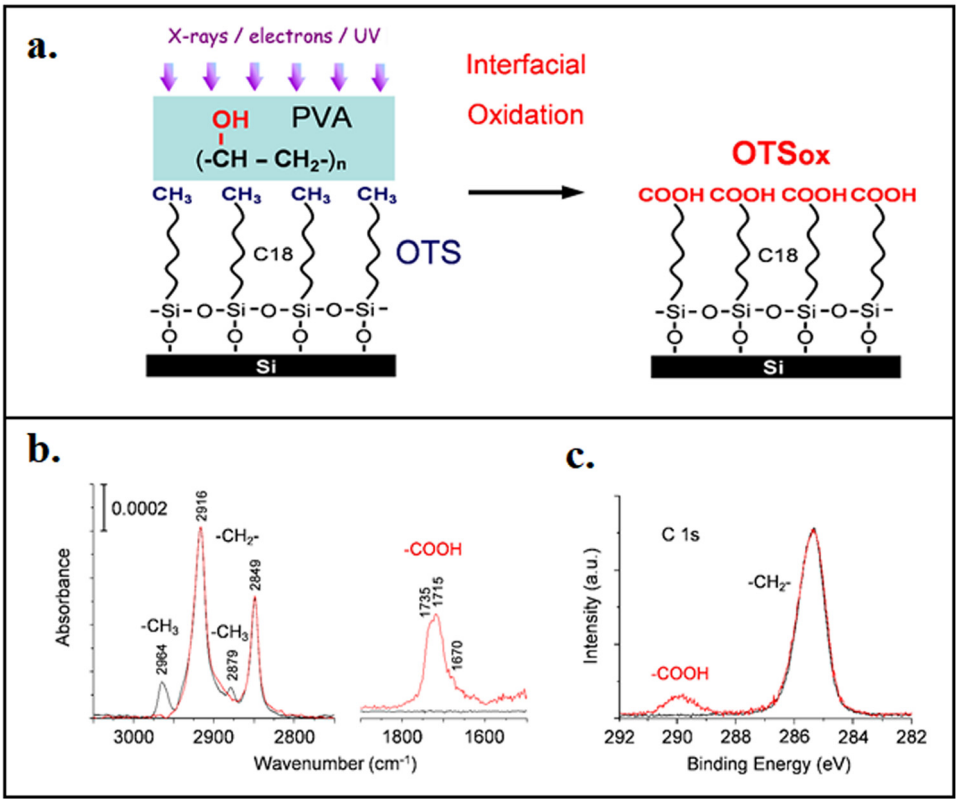

Fig. 6 Interfacial beam-induced chemical transformation. (a) Schematics of the molecular structures in interfacial solid-phase oxidation of an OTS/Si monolayer to OTSox/Si, using a thin PVA film as an oxidation reagent. Irradiation means (X-ray, electrons, UV) used to activate the process are indicated. The bare OTSox surface is revealed upon *ex situ* removal of the PVA film. (b) Quantitative Brewster angle FTIR spectra of the pristine OTS/Si monolayer (black) and the irradiated monolayer after removal of the PVA film (red). (c) XPS C 1s line, as recorded from a pristine OTS/Si monolayer, before depositing the PVA film (black), and from the X-ray irradiated PVA-coated OTS/Si, after complete removal of the irradiated PVA film (red). Peak heights in panel c are normalized for visual convenience. Note the combined XPS and FTIR indications for COOH formation upon XPS irradiation, while the CH_3 signal in FTIR vanishes. Taken from ref. 94.

research. The schematics of the molecules are given in Fig. 7b. Two batches (sets I and II) of alkane chains were used, four samples in each, with varied length, n = 6, 8, 10, and 16, plus a third set (III) of three di-phenyl molecules, denoted S, D and T, referring, respectively, to the type of linkage between the two rings: a single, double and a triple bond. For all systems, the band diagram consisted of a vertical surface field that acted to push holes from CdSe to gold, as illustrated in Fig. 7c, bearing only slight variations between samples. Therefore, the PV sign was expected for all samples to reflect electron accumulation at the NPs as soon as light was switched on. Moreover, subject to trivial arguments, the PV magnitude was supposed to increase upon decreased charge transport efficiency and, in turn, the PL magnitude was expected to exhibit a tendency opposite to PV, because PL scales with the amount of (excited) electrons and holes that remain within the NPs.

The measured results, however, were far from any naïve expectation. First, the PV and PL magnitudes were not always of opposite trends. Second, in some samples, extra positive charge was found to accumulate under illumination, see, for example, set I in Fig. 7g. Third, the dependence of PV magnitude on spacer thickness was not necessarily monotonic and, once a correction term was employed (common to the entire set, see below), it obeyed indeed the expected exponential dependence; however, for hole accumulation other than electrons, see Fig. 7h.

A simple model based on rate equations for the population of electrons, f_e, and holes, f_h, at the NPs was therefore employed. The coupled equations, eqn (9)a and b, consist of three terms each, where the constants of both generation rate (normalized to be = 1) and recombination rate (k_{rec}) are identical for electrons and holes. Differences between electron and hole dynamics are expressed solely by the term of transport to the gold, with respective rate constants k_e and k_h.

$$\frac{\partial f_e}{\partial t} = (1-f_e)(1-f_h) - k_e f_e - k_{rec} f_e f_h \quad (9a)$$

$$\frac{\partial f_h}{\partial t} = (1-f_e)(1-f_h) - k_h f_h - k_{rec} f_e f_h \quad (9b)$$

A reasonable form of k_e and k_h such as to account for the tunneling across a spacer may be: $k_i = A_i \exp(-\beta_i L)$, where L is the spacer width and β_i are the tunneling-related attenuation parameters. The steady state, namely the solution for $t \to \infty$,

yields quantities that can be compared with experiments: (1) the total charge on the NPs, Q, and (2) the PL intensity, I_{PL}, where:

$$Q \sim f_h - f_e \quad (10a)$$

$$I_{PL} \sim f_h f_e \quad (10b)$$

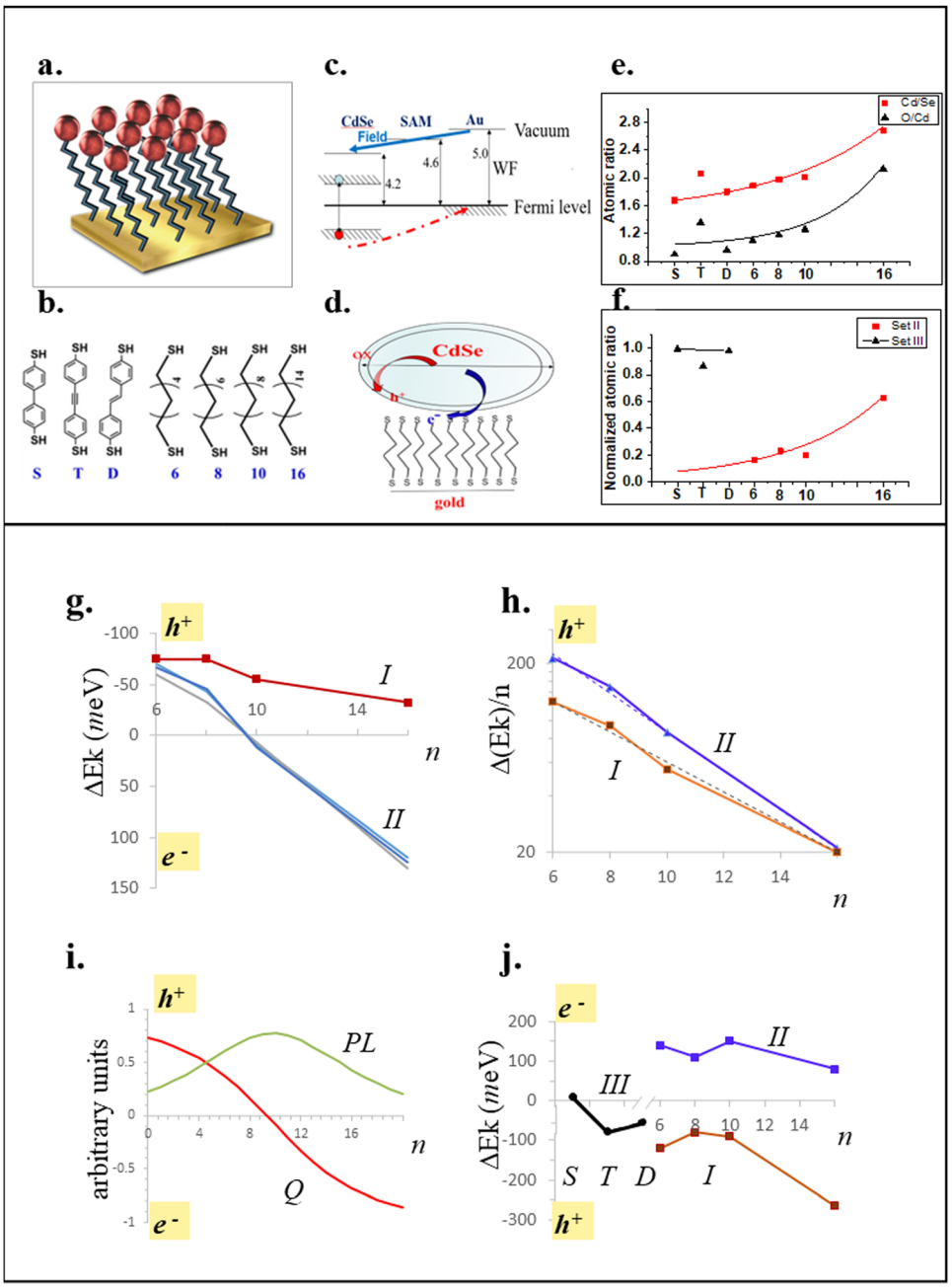

Fig. 7 Dithiol SAMs on gold. Top: (a) Schematic of the monolayer assembly on gold, with post-assembly deposited CdSe nanoparticles on top. (b) Seven types of molecules used for the formation of SAMs, including four alkane chains of varied length and three di-phenyls of varied conjugation strength. (c) Schematic of the band diagram, consisting of a vertical surface field (common to all systems) that promotes (rejects) hole (electron) transport from CdSe to gold. (d) Schematic of the dominant charge traps found in these systems. (e) Experimentally evaluated nanoparticles' oxidation, expressed in terms of Se deficiency (Cd:Se) and the total oxygen content (O:Cd). (f) Evaluation of the chemical attack at the top-S sites prior to the deposition of nanoparticles, expressed in terms of S^{top}/S^{bottom} ratios; values already corrected for photoelectron attenuation such that all ratios should ideally be =1. Bottom: (g) Measured PV values of the alkane-chain-based samples, showing considerable differences between alike sets, I and II. Note the 'strange' behavior of set II, obtained consistently in repeated experiments. (h) PV values of panel g, translated into charge magnitudes, however with a fixed term of trapped charge added to all samples in set II (note that, common to both sets, an approximate exponential dependence on n is thus revealed). (i) Simulated charge (Q) and photoluminescence (PL) magnitudes that successfully reproduce the results obtained from set II. (j) CREM tests of dominant charge traps, showing that set II consisted indeed of dominant electron traps while hole traps dominated the other sets. Positive (h^+) and negative (e^-) charge domains are indicated at all panels. Taken and reorganized from ref. 106.

Based on this model, it is possible to reproduce the accumulation of holes, including its exponential dependence on chain length, L, as observed with the sets of alkane chain-based molecules, sets I and II (see in particular Q in Fig. 7f, which reproduces the behavior of set II in panel Fig. 7g). Interestingly, however, the parameters used to get this result reveal pronounced differences between holes and electrons in their attenuation parameters, β_i, as well as the corresponding pre-factors, A_i, of the transport rate constants, $k_i = A_i\exp(-\beta_i L_i)$. As expected, the difference in β_i is consistent with the band diagrams derived *in situ* and schematically illustrated in Fig. 7c. However, the huge difference in A_i values indicates a feature not accounted for by the model: a competing process of charge trapping, found eventually to occur at sites exterior to the photoactive NPs. Such charge capturing mechanisms would necessarily affect the A_i pre-factors *via* grabbing charge into traps and, obviously, they should also affect the measured PV and PL magnitudes. Upon fitting to the PV and PL experimental results, the pre-factor turned out to be extremely large for electrons, as compared to holes. Moreover, the A_i pre-factors successfully reproduced differences between different batches of alike samples, see set I and set II in Fig. 7g, pointing to trap densities. Hence, a following question could be raised, whether the origin of these traps could be further revealed.

Useful input in this regard was obtained from the standard XPS evaluation of the quality of SAMs, before and after depositing the CdSe nanoparticles. In general, high-quality SAMs were consistently formed, except for the top S-atoms of the dithiols, S^{top}, which were found to occasionally suffer oxidative attack and, as a result, partial evaporation. Detailed analysis can be found in the Supplementary Information of the original paper.[106] A second type of defects was observed in the CdSe nanoparticles. Their surface coverage was found nearly complete and reproducible, but some oxidative passivation at the nanoparticle shell appeared in different amounts for different samples. Fig. 7e and f present a quantitative summary of these defects for selected sets of samples.

Independently, based on dedicated tests at the very early stages of sample exposure to the X-ray beam, it was shown that, effectively, the passivated shell of NPs introduced hole traps, while the attacked S^{top} sites served as electron traps, see illustration in Fig. 7d. As shown in Fig. 7j, all set II samples were dominated by electron traps, whereas set I and set III were dominated by hole traps. Fig. 7i presents the simulated PV and PL results for the four samples in set II, with an account of the effect of trapping on A_i pre-factors. These combined results explain the 'strange' PV-dependence on chain length in the set II samples, Fig. 7g, for which transport of electrons to the gold was indeed disfavored by the surface field, but at the same time competing trapping mechanisms were of significant role.

The role of charge traps turned the interpretation of PV and PL data considerably more complex. Needless to say, this is a well-known difficulty in molecular electronics. Yet, the combined chemical and electrical data present a consistent collection of results, explaining successfully the behavior of all three batches of samples by expressing explicitly the charge trapping role, in addition to the pre-designed spacer parameters. This case demonstrates how detailed understanding of the SAM-nanoparticle interface, as well as the interface of each of those with the vacuum, can become essential for getting a comprehensive description of measurement results. While this conclusion is indeed trivial in any context of electrical measurements, its relevance to systems consisting of organic molecules seems to be of particular importance.

Notably, as shown in Fig. 7e and f, a systematic spacer-dependent trend to form defects was observed: the NP passivation depended on the alkane chain length and, in contrast, an opposite systematic trend was noted for the S^{top} degradation. This observation indicates that a remote role was played by the gold substrate as a protecting or accelerating support, against/for chemical attacks, for which the spacer served as an attenuator. Literature reports on such effects are consistent with this observation.[107] In contrast to the light-induced measurements discussed above, the latter trends regard charge transport at dark, chemically driven.

5.2. Dense packing of conjugated molecules

The conjugated molecules, S, T and D, were intentionally chosen because they presented varied conjugation between the two phenyl rings within each molecule, with yet only small differences in molecular length. Two intriguing assembly issues were revealed. While D exhibited 'normal' assembly characteristics, both S and T presented unusual effective thickness values. Standard thickness calculation of the bare SAMs, prior to CdSe NPs deposition, was based on the XPS-measured ratios of C/S, C/Au and S^{top}/S^{bottom} signals and, in reference, on calculated ratios for perfect layers, employing attenuation factors atom by atom. For the SAM of S-molecules, this analysis suggested a very compact arrangement. Namely, the layer thickness could perfectly fit the theoretical molecular length, provided that the amount of material was increased *via* dense packaging. Supposedly, π–π interactions between the phenyl rings of neighboring molecules could overcome the natural conformation of a free molecule, in which the two rings are oriented in perpendicular planes. By aligning both rings along the same plane, the increased layer density is enabled sterically, hence energy is gained *via* (1) the formation of additional S-Au bonds; and (2) the formation of stronger interactions between phenyl rings of neighboring molecules. A schematic drawing of the suggested arrangement is shown in Fig. 8a.

Remarkably, such a compact in-layer arrangement should be expressed by the photoelectron attenuation length parameter, denoted here as λ;[108] a phenomenological constant that usually requires extensive experimental work to be extracted.[17,109] Indeed, the calculated value of λ in this case was pronouncedly small, about 70% of the value extracted for the D molecules (recall that the effect of λ is *via* an exponential term). The importance of this result stems from the fact that compositional XPS analyses are affected by and rely on literature-provided attenuation parameters. System-specific λ-variations, fitted to the huge diversity of specific samples in routine XPS works are mostly unavailable in the literature. The present work

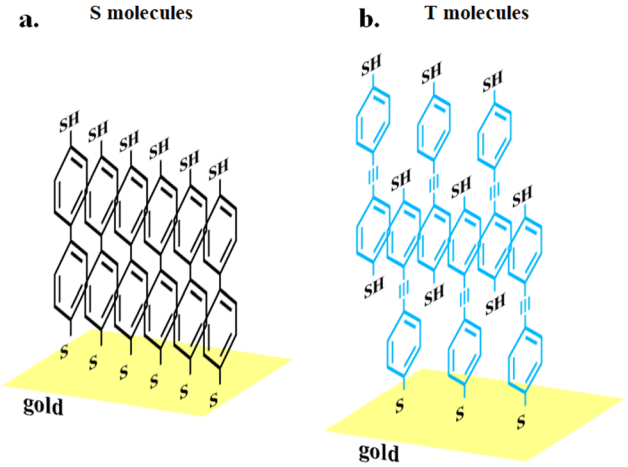

Fig. 8 Self-assembly of conjugated dithiols. Schematic of the assembly arrangement in SAMs of the conjugated S (a) and T (b) molecules.

proves that such variations should be considered thoroughly for interpretation correctness and quantification accuracy, in particular when organic molecules are investigated. Detailed analysis of the present system can be found in the SI file of the original paper,[106] showing inner consistency and high reliability of the results and their interpretation.

A second non-trivial assembly feature was noticed for the T-molecules. Repeatedly, they were found to form a double layer instead of a monolayer. Evidence was twofold: the total layer thickness was too high and, independently, too many of the S-atoms were not bonded to gold. Aided by the theoretical calculation of attenuation, as mentioned above, two organization solutions for the second T-layer were thus found to retain consistency with all XPS pieces of data. Both solutions assumed the formation of a complete first layer, and either (1) a second layer was formed on top, however with slight deficiency in compactness, $<20\%$, or (2) a second layer was incorporated at half height in between the molecules of the first layer, as illustrated in Fig. 8b. Energy gain in the latter option is expected to be higher, as it includes both the formation of π–π interactions between neighboring rings and an attractive interaction between free SH groups and the triple bond. Therefore, it is proposed that the T-molecules form another type of a 'perfect' assembly, in which strong intermolecular interactions are enabled. Interestingly, the only molecules that did not materialize such an energy gain were the D-molecules, a result attributed to steric disturbances introduced by the tilted C=C bonds.

Based on the structural insight gained from the XPS analysis for the conjugated molecules, electrically expressed differences between D-, T- and S-SAMs were expected to show up as well, because induced potentials at the CdSe NPs should depend on the spacer's dielectric constant, ε. As already mentioned, inherent differences in the polarizability of the single molecule in this set of samples are expected from the variations in linkage between the two highly polarizable phenyl rings, as shown in Fig. 7b. However, except for those, as an assembly feature, ε variations expressing the collective dielectric response of many molecules should be considered. To start with, S^{top} oxidation was practically absent from the conjugated SAMs, suggesting that the chemical drive (at dark) for charge transport from the gold to the top site was suppressed by increased polarizability of the spacer, in agreement with the measured compositional data. Second, in spite of the minor differences in molecular length between D, T and S, their PV (not shown) and ΔE_k magnitudes in Fig. 7j exhibited significant differences. It would be very difficult to explain these results without the structural input gained by the compositional analysis. In turn, by transforming the PV data into charge magnitudes, with the extra thickness of T taken into account, a reasonable monotonic tendency was obtained, reflecting variations in ε. The estimated changes in ε (compared to ε of the D-layer) yielded a factor of $\sim$1.4 for the T-layer and $\sim$2.6 for the S-layer.[110]

Consequently, this set of experiments on seven different SAM-spacers demonstrate some of the added values gained by assisting the interpretation of electrical data with *in situ* structural input, and *vice versa*. CREM-wise, the PV measurements yielded local responses to light; local in the sense that by detecting the Cd line-shifts, the ΔV values are averaged over many particles but, yet, not with contributions from ex-particle domains. In addition, use was made of dedicated *in situ* work-function measurements,[38,70,111] as inputs for the band diagrams and, importantly, as an indicator of dominant charge traps in each sample, as shown in Fig. 7j. Additional CREM modes are discussed below to further demonstrate how the combined chemical and electrical information of CREM-XPS enables detailed understanding that is hardly even approached by any single technique.

6. Molecular gates in bacteriochlorophyll

In a study of yet small molecules, however of a clear biological relevance,[112] another interesting aspect of the CREM capabilities was demonstrated: the charge injection issue. As already mentioned, standard electrical measurements are based on the attachment of electrodes *via* two or more physical contacts to a sample. CREM works without the need in top contacts, which affects the readout capabilities, but also the signal-in mechanism: the charge-injection. By using an eFG, the electrons supplied to the sample, even if set to nearly zero kinetic energy, are very 'hot' in reference to the Fermi level, with energies above the vacuum level. Therefore, they are expected to behave differently than electrons injected around the Fermi level by a standard electrode. The resulting CREM sensitivity to hot-electron characteristics presents a very important and unique feature, as indeed exemplified by the study described hereafter of bacteriochlorophyll (BChl) derivatives.

Self-assembly on Si-wafers was conducted for two such molecules: non-metalated (denoted 2H) and Pd-metalated (Pd) bacteriochlorophyll analogues, shown in Fig. 9a and b. Sample characterization by a variety of techniques can be found

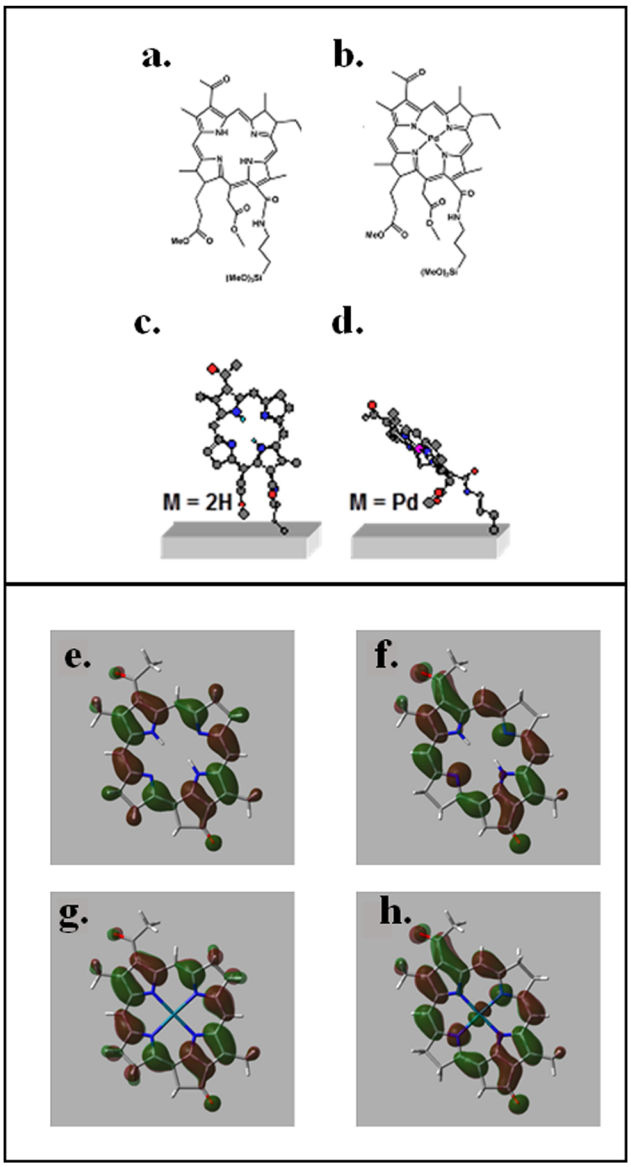

Fig. 9 Molecular structures (top) and selected orbitals (bottom) of the BChl derivatives. Top: Molecular structure of nonmetalized (2H) BChl (a) and metalized (Pd) BChl (b). Assembly on Si substrates of the siloxane-based monolayers: 2H–BChl (c) and Pd–BChl (d). For visual clarity, alkyl groups are omitted and the macrocycle of 2H–BChl is drawn parallel to the plane of the page, whereas that of Pd–BChl is drawn on a perpendicular plane, thus highlighting the average tilt of Pd–BChl with respect to the surface normal. Bottom: (e–h) Calculated molecular orbitals employing the hybrid B3P86 functional for density functional theory in combination with the SDD basis set, using Gaussian 03, presenting HOMO and LUMO of 2H–BChl ((e) and (f), respectively) and of Pd–BChl ((g) and (h), respectively). Negative and positive densities are denoted by green and brown colors, respectively. Figures were produced using GaussView 3.09. Taken from ref. 112.

in the original papers,[112] showing the formation of high-quality SAMs, with one notable observation: the 2H SAMs were formed with the molecules being vertically oriented, whereas the Pd-SAMs consisted of molecules tilted with respect to the surface normal, as shown in Fig. 9c and d. The CREM experiments

Table 3 Four operation modes in CREM, sorted with respect to the charge injection means and the background surface field that is pre-stabilized *via* the accumulated extra charge, Q. Taken from ref. 112

	Probe	Field direction	Excited state	Excited state symbol
1.	eFG	$\downarrow Q < 0$	Electron injection	e
2.	eFG	$\uparrow Q > 0$	Hole annihilation	h
3.	Light source	$\downarrow Q < 0$	Electron-hole creation	e–h
4.	Light source	$\uparrow Q > 0$	Electron-hole creation	e–h

explored four qualitatively different signal-in cases, described in Table 3: two non-neutral sample states, positively or negatively charged, to which two types of irradiation were applied, photons at 630 nm, or low-energy electrons. Based on the comparison between different charge injection means, it was possible to extend and cross-validate our understanding of the molecule-hot-charge interaction and mechanisms, with a specific focus on the differences emerging between different molecular sites.

The available potential changes (denoted here by Δ) at sub-molecular levels were mainly those derived from the N 1s, Pd 3d and C 1s line shifts. The first two provided information on the center of the molecular macrocycle. In turn, the C signal, which is dominated by atoms distributed over the periphery of the molecule, informed on the 'out of center' changes in electrostatic potential. Due to finite impedance at the back contact, the Si-wafer and its native oxide were also examined electrically, such that back impedance contributions could be removed by direct evaluation of the actual potentials developing underneath the SAM.

Fig. 10a and b present the response of these monolayers to red light. It was found to be quite similar for both SAM types, 2H and Pd, reflecting electron transfer from the molecular periphery to its center. Practically, this periphery-to-center electron transfer is expressed by the element-specific magnitudes of Δ, yielding for N (and Pd) larger values than for C. Differences between the 2H- and Pd–BChl in absolute Δ magnitudes are of minor importance in the present context, attributed to the photoactivity of the Si substrate itself. It is noteworthy that in order to get the SAM-relevant information, substrate-related Δ-values should be subtracted, as indicated by the dashed lines in the figure. Then, the net molecular results agree with the calculations of HOMO and LUMO orbitals, Fig. 9e–h, in which the LUMO spatial distribution is more confined to the molecular center, as compared to the HOMO distribution.

Panels (c) and (d) in Fig. 10 present the response to fine electron injection under initially positive charging conditions. The experiment is tuned to examine hole-annihilation processes *via* hot-electron injection. The results were essentially consistent with expectations, bearing nuances that are not of much interest in the present context, except for the fact that the introduction of Pd gave rise to slight differences between the center of the molecule (N, Pd) and its periphery (C); differences that are not seen in the 2H samples.

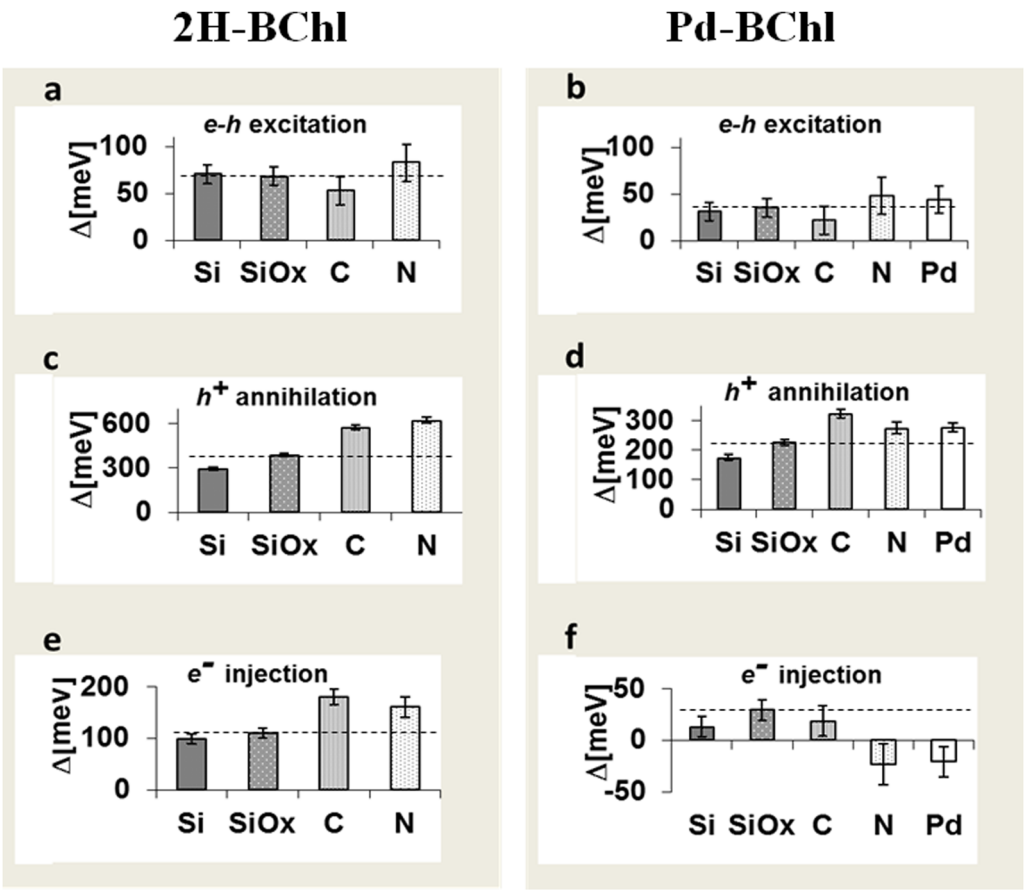

Fig. 10 Selective charge injection experiments. Raw XPS line-shifts in 2H–BChl and Pd–BChl, respectively, as obtained under light illumination (a) and (b), $Q > 0$ eFG application (c) and (d), and $Q < 0$ eFG application (e) and (f). All BChl site-specific potentials float on that of the substrate, as indicated by dashed lines, which should eventually be subtracted to get the relevant molecular response. Error bars were determined based on the variations encountered upon repeated measurements, combined with the experimental error in derivation of a single shift. Adapted from ref. 112.

In contrast to the above, panels e,f in Fig. 10 present a very unusual result, with regard to hot-electron capturing: while the 2H sample underwent an increase in electron density, as expected under the flux of external electrons, the Pd-SAM showed repeatedly and consistently an absolute depletion in electron density at the molecule center. This result, similar to negative differential resistance (NDR), is remarkable because the supply of large amounts of extra electrons could be verified by measuring directly the current on sample's back contact, as well as by the additionally measured elemental Δ-values. To make a point clear, even if none of those injected electrons was captured around the Pd center, it would not be sufficient to get a definitely opposite response. The research question was therefore focused on the mechanism leading to (local) depletion in electron density under exposure to a flux of external electrons.

Physical insights into this puzzling question were gained from DFT-based computations of the polarizability perpendicular to the molecule plane, conducted for the single isolated molecules. Computationally, variations in the local electron density under an applied external field were derived as a function of distance from the molecular plane above the selected atomic sites, as shown in Fig. 11a–c. A pronounced maximum was thus found at $\sim$5 A above the metallic center, see Fig. 11a and b, with a clear difference from the 2H case, Fig. 11c. This feature expresses the capability of Pd–BChl to donate electrons under external fields. As such, it accounts for the experimental result since, effectively, under the CREM experimental conditions, a high surface field is stabilized. It also turned out, based on X-ray reflection (XRR) plus XPS data, that the actual distance between the Pd site and the substrate was about 6 A, very close to the calculated maximum in molecular polarizability.

Further computations for molecules in the gas phase were conducted to examine the question of dimer formation. For 2H–2H dimers, as well as Pd–Pd dimers, optimal dimerization was obtained in the parallel orientation of the two molecules, as shown in Fig. 11e. However, for the 2H–Pd pair (Fig. 11f), the optimized structure obtained by these computations was very different and, remarkably, very close to a known natural structure: that of cofactors that appear in a variety of biological systems, all over the evolutionary branches and, in particular, in a chlorophyll site located between the photon absorption center and the photosynthesis reaction center. Similarity

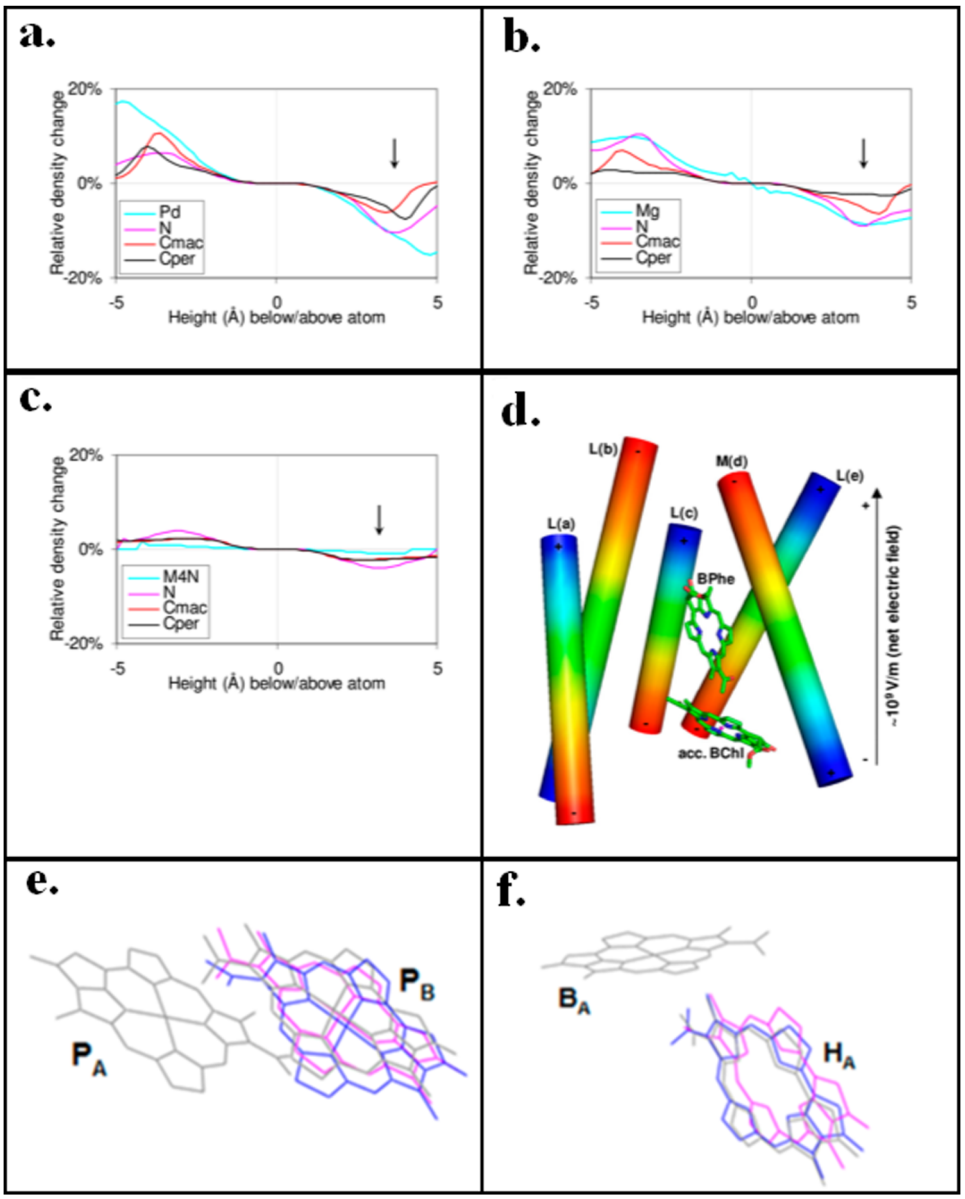

Fig. 11 Computations for the BChl analogues. (a–c) Changes in electron density (relative to the unperturbed density), plotted for selected molecular sites (C_{mac} = carbon in the macrocycle, C_{per} = carbon in the periphery, M4N = center of 4 N atoms in 2H–BChl), as calculated along a perpendicular axis from 5 Å above (+5) to 5 Å below (−5) the macrocycle plane. Molecules Pd–BChl (a), Mg–BChl (b), and 2H–BChl (c) display the electric field effect on electron density perpendicular to the plane under constant and uniform external field, 0.0025 au, or $\sim 1.3 \times 10^9$ V m^{-1}. The pronounced extrema in panels a and b, relative to panel c, are highlighted by arrows. (d) Arrangement of the reaction center (RC) bacteriopheophytin (BPhe, 2H–BChl) and accessory BChl (Mg–BChl) with respect to their surrounding α-helices in the bacterial RC. The helix dipoles are denoted in blue (positive) N-termini and red (negative) C-termini and their cumulative field is $\sim 10^9$ V m^{-1}. (e and f) Calculated optimal geometry, relative to the crystal structure (gray), of dimerization of two M–BChl molecules (e), where M is either Mg (magenta) or Pd (blue), and of the mixed dimer (f). The geometry for the $(2H–BChl)_2$ dimer (not shown) is similar to the one in panel (e), however a different geometry is obtained for the mixed dimers (f), Mg–BChl-BPhenyl (magenta) or Pd–BChl–BPhenyl (blue). Taken from ref. 112.

between the computed and natural structures applies for both the relative orientation and the ∼5 A distance between the metal site (Mg in the Natural system) and the peripheral site of the 2H molecule. Recalling that Nature exploits self-assembly at all levels, this latter computation sheds light on the question 'why these cofactors are so evolutionary robust and common'.

Moreover, insight into the function played by these cofactors was gained in this study. The combined CREM data and polarizability calculations demonstrate as a whole that the cofactor presents 'gates' for efficient electron-in and electron-out transfer. Arranged in the relative positioning described above, this function is optimized, such that it can assist unidirectional electron transfer. The calculations further showed that Mg is the best divalent cation to provide the gate-out feature. Therefore, proven by this study, the structure–function relationships of these cofactors appear to be

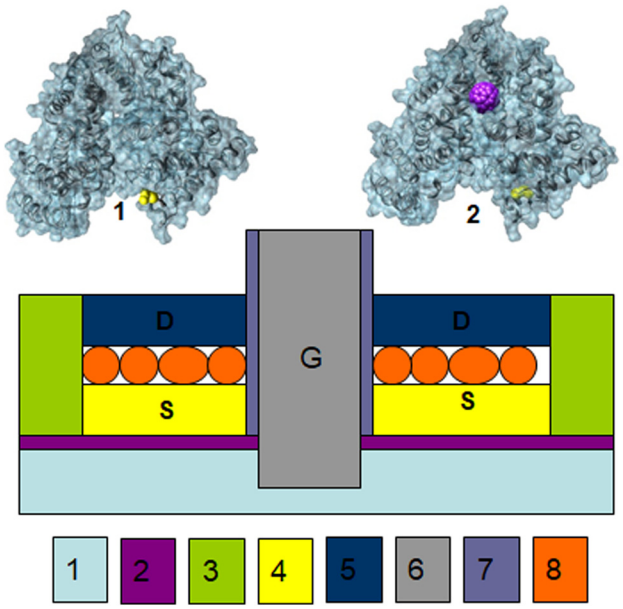

Fig. 12 The molecular vertical transistor (MolVeT) device. Top: Schematic of the un-doped (1) and C_{60}-doped (2) bovine serum albumin (BSA). Bottom: C-Gate MolVet structure. The vertical transistor is formed inside a micro-cavity comprising highly doped silicon (1) covered with silicon dioxide (2) and surrounded by a silicon nitride layer (3). Au (4, Source), Pd (5, drain) and oxidized Ti (6,7, gate) electrodes are used to activate the protein layer (8) in the miniature junction.

optimized in a meticulous detail during the 3.5 billion years of evolution: molecules self-arrange *via* electrostatic forces, hence structure is determined at an electrostatic equilibrium, whereas the biological function emerges out of this equilibrium, being based on the molecular polarizability. This observation of co-optimized structure and function *via*, respectively, the equilibrium and dynamic characteristics, is believed to be of considerable generality. In the present case of chlorophyll cofactors, the structure is designed to collectively focus the polarizability function onto an optimal distance above a specific molecular site, which exemplifies one of the 'sophisticated' ways Nature constructs bio-devices on the molecular scale.

A question may yet be raised as of the apparent differences between CREM experimental conditions and the Natural environment, regarding, for example: (1) the UHV (ultrahigh vacuum) XPS conditions; (2) the CREM charge injection means; and (3) the metal probe utilized. However, it turns out that, in all these aspects, the natural process is closely imitated by the experiment. First, the relevant environment within the chlorophyll is locally dry, consisting of sub-nanometer empty spaces around the molecules. Second, a global controllable field is stabilized in CREM, similar to the field produced by proteins within the chlorophyll. Third, the CREM charge injection means correspond very well to the hot, photoexcited electrons in chlorophyll, perhaps even better than those of alternative, commonly used, *ex vivo* techniques. Finally, the functional properties of Pd derivatives present close similarities to those of Mg derivatives, even though differences should not be overlooked.[113]

7. BSA protein-based miniaturized devices

7.1. Transistor devices with and without C_{60}-doping

A research project aimed at the incorporation of biological molecules in electronic devices is described in this section.[96,114] This ambitious attempt was motivated by features typical to bio-macromolecules, such as recognition, self-assembly,[115,116] robustness at the nanoscale and the sophisticated charge manipulation mechanisms exploited in Natural systems. Bovine Serum Albumin (BSA, Fig. 12 top), a protein macromolecule of considerable biological importance, is known to effectively bind small molecules (mainly hydrophobic ones) and, also, to form robust SAMs on gold. Unlike certain types of metalloproteins that are involved in biological electron-transfer processes (such as azurin and cytochrome-*C*), BSA has no central redox center, but a variety of active sites. Therefore, doping the BSA with redox molecules was investigated, and SAMs were formed in a procedure described elsewhere.[117] In particular, doping with C_{60} molecules was found to selectively target a specific BSA site with a strong acceptor-like character (tryptophan, Trp214 in subdomain IIA, see Fig. 14b).[118,119] Additional dopants, such as tetraphenyl-21*H*,23*H*-porphine (TPP) and its Cu and Fe metallo- derivatives (TPPCu; TPPFe respectively), were also tested.[117,120]

The successful construction of BSA-based junctions in miniature transistor devices, shown in the scheme in Fig. 12, is a remarkable achievement by itself, demonstrated for both un-doped and C_{60}-doped BSA.[114,121] Yet, the interpretation of device characteristics encountered a variety of critical unknowns. The source-drain *I–V* curves of un-doped and C_{60}-doped BSA (Fig. 13) present clear rectification characteristics, favoring electron conduction as verified from the dependencies on gate voltage (V_G).[122] Besides questions on structural details and stability issues, the function of BSA as an electrical component was intriguing, raising questions on: (1) the reason for rectification; (2) the mechanism giving rise to a strong C_{60} effect on the e-conduction, while having no effect on h-conduction; (3) the *I–V* curve which obeyed $I \sim V^{\alpha}$ for C_{60}-BSA, with $\alpha = 2$, was markedly different in the un-doped BSA, with gate-voltage-dependent α, yielding values between 2 and 5; and (4) the interpretation of transport data in terms of specific molecular groups and their spatial arrangement; to mention just a partial list.

Helpful inputs were provided by the XPS-CREM data, extracted from large-area SAMs without the Pd top electrode. Fig. 14a presents the CREM *V–V* curves of O and C. The potential developing in the layer, as expressed by ΔE_k of these elements (also *N*, not shown), is plotted as a function of the sample bias, V_B. The experiment was conducted under fixed eFG conditions and low X-ray flux, while the sample bias was set initially to high negative values, then step-wise decreased

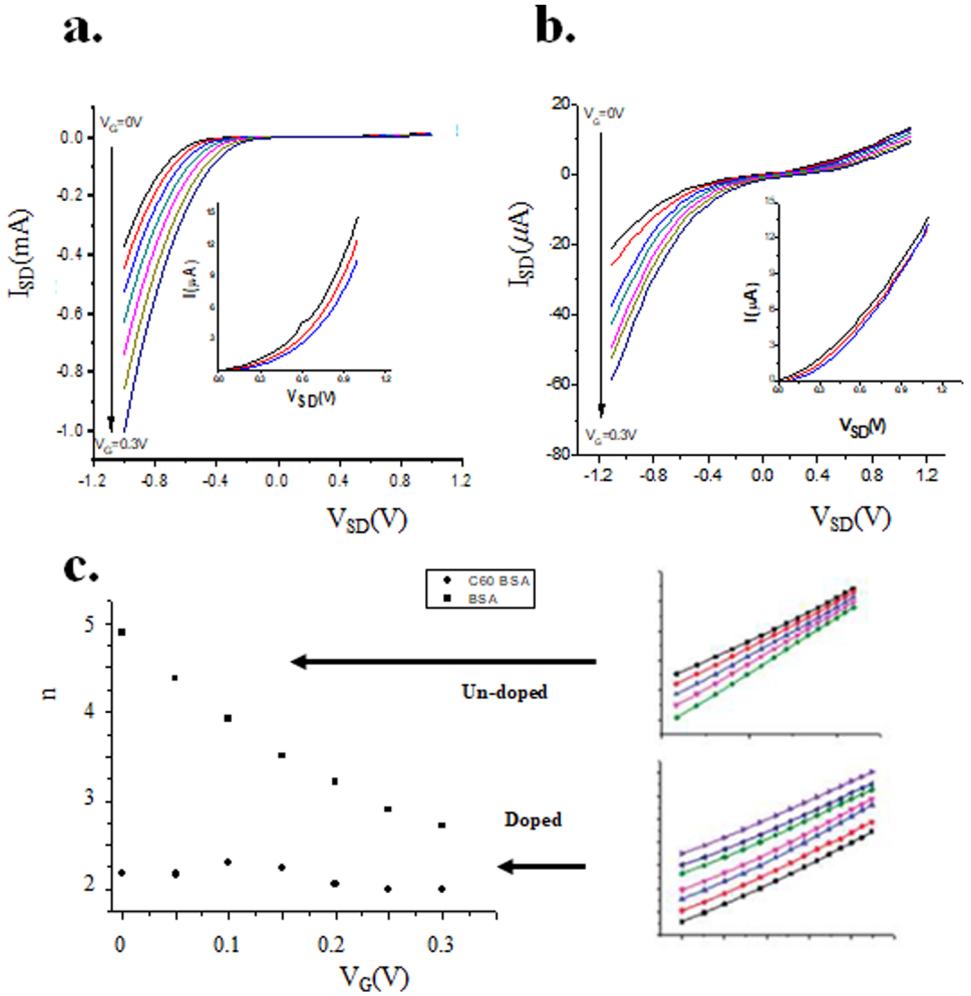

Fig. 13 Transistor device transport measurements. Source–drain I_{SD}/V_{SD} of the un-doped (a) and doped C_{60}-BSA (b) devices, as a function of gate voltage, V_G. Main panels (insets) show I–V curves recorded under negative (positive) V_{SD}. Note how the current magnitude increases (decreases) under negative (positive) polarity as V_G is increased (V_G step size = 0.05 V), pointing at electron (hole)-dominated transport mechanisms. (c) The negative-polarity exponent factor (α) as a function of V_G (left) in BSA (■) and C_{60}-BSA (●), derived from the log–log I–V plots on the right panel. Taken from ref. 96.

until reaching a certain value, set such as to prevent exposure to elevated e-fluxes and thus avoid irreversible sample modifications. Finally, the bias increments were reversed, back towards increased negative values. Similar to the I–V demonstration in Fig. 2c, an inflection point (IP) is noted in these curves, at the bias for which incoming electrons overcome the potential barrier and start landing on the surface. At a sufficiently high negative bias, prior to reaching IP, samples tend to charge up positively due to the X-ray irradiation. For lower negative bias values, enabling a flux-in of electrons, they would normally accumulate negative charges, as indeed seen for the curves in Fig. 14a.

Importantly, the sample work-function (WF) can be derived from the measured IP,[111] yielding 4.35 eV for un-doped BSA and 4.7 eV for C_{60}-BSA.[123] In the device, the WF of both electrodes, Au and Pd, is higher, around 5.0 eV, which suggests the spontaneous formation of interfacial barriers of similar heights at both sides of the BSA layer. Therefore, recalling the pronounced rectification features observed in Fig. 13, an inner BSA field was considered as a feature that broke the symmetry between top and bottom electrodes. It was associated with the spontaneous formation of space charge. Hence, inner fields, upon contact with metal electrodes, become vertically oriented within the BSA layer. The detailed distribution of space-charge appeared to be affected by the C_{60} doping, due to changes in the spatial distribution of those sub-BSA groups that could take active part in charge reorganization. As indicated by WF values, the total field in the C_{60}-BSA layer was about half of the one in un-doped BSA and, accordingly, upon C_{60} doping, the asymmetry between electron- and hole-conduction was indeed reduced.[124]

It is noteworthy that in Fig. 14a, the hysteresis manifested by the CREM V–V curves is quite similar for different elements in a given sample. However, pronounced qualitative differences are observed between the two samples: For C_{60}-BSA, very large hysteresis is observed, while the un-doped BSA exhibits a rather regular behavior. Forward and backward directions in the V_B-scan are indicated in the figure, showing that un-doped BSA can store negative charges, whereas C_{60}-BSA does not 'allow' negative charge storage (no hysteresis at the section of negative

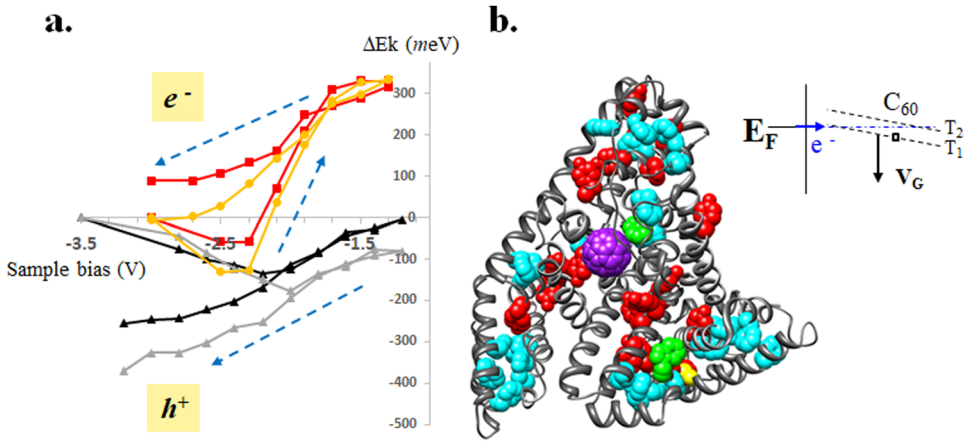

Fig. 14 CREM of BSA - the effect of C_{60} doping. (a) CREM *V*–*V* loops, plotting ΔE_k of O 1s and C 1s lines in un-doped (yellow-O, red-C) and C_{60}-doped (grey-O, black-C) BSA under varied sample bias. All curves start at their $\Delta E_k = 0$ datapoint. Blue arrows indicate the chronological order of measurements. Regimes of electron (top) and hole (bottom) accumulation are indicated. (b) Patchdock simulation of the molecular structure of C_{60}-BSA with its leading acceptor (phenylalanine, light blue) and donor (tyrosine, red) sites. C_{60} (violet), the tryptophan sites (green), and the cysteine binding group (yellow) are also indicated. For this orientation of the molecule, the gold electrode would be located underneath and the Pd electrode above the molecule. A 3D movie presentation of the molecule is provided in the Supplementary Information of the original paper. The inset (right side of the panel) illustrates the effect of positive grid bias on the active trap states, T_1 and T_2 (separated by ~350 meV), to which C_{60} introduces a mandatory discontinuity in real space. Note in panel (a) the pronouncedly different hysteresis at the two samples. Adapted from ref. 96.

charge accumulation). In turn, it presents remarkable affinity to positive charge storage (huge irreversibility at the positive charging section).

As C_{60} is a well-known electron acceptor, it would be interesting to understand why and how the C_{60} doping leads to such a strong hole trapping behavior. An answer is believed to be given by the complexation process. The incorporation of a Fullerene molecule within BSA, prior to the formation of metal contacts, involves electron transfer to the dopant, donated mainly by tyrosine groups and the nearby tryptophan at the Trp214 site. This enrichment in electron density switches the affinity of this site, turning it into an efficient hole absorber. Quite likely, this very charge redistribution also affects the charge mobilization upon thermodynamically equilibrating with the metal electrodes, such that the effective inner dipole within the SAM is reduced.

Moreover, related to the issue of charge capturing, upon hosting a C_{60} molecule at Trp214, this site loses its dominant role in electron conduction, namely as a hoping site for electron transport mechanisms. Based on studies of the BSA structure, one can identify the favorable routes (real-space) for electron hopping across the molecule, being dominated by phenyl groups and the Trp214 site at subdomain IIA. The latter site, however, is unique in the sense that it is 'strategically' located at a central position through which most efficient paths go.[125] By blocking this site upon C_{60} incorporation, most of the leading conduction routes for electrons are affected and the only ones remaining available are those taking longer paths along the peripheral sites of the molecule.

Therefore, it is the combination of a chemical change and its specific location that explains why electron transport is so highly influenced, in contrast to the negligible effect on hole transport and in spite of the small size of C_{60} as compared to the protein macromolecule. Expressed in terms of trap states in a semiconductor, the original paper further correlates between the energy diagram and the structural information. Fig. 14b explains the pronounced variations in α-values of the un-doped-BSA curves by means of an energy spread, about 350 meV in magnitude, between trap states that take active part in the electron transport, T_1 and T_2. As soon as the C_{60} doping blocks a central T_1 trap site, the related α-variation reduces to a strict value, $\alpha = 2$, typical of 'charge-limited' transport mechanisms.

An intriguing question is raised by this study regarding the possible relevance of such results to any of the biological functions of BSA. Obviously, the solid-state BSA realized upon assembly on gold, out of the aqueous solution, presents a system very different from any of the biological ones. And indeed, as further discussed below, critical questions on dehydration and related conformational changes are encountered in the solid-state phase of BSA. Yet, the observed switch in affinity at subdomain IIA proposes a functional similarity to the corresponding bio-systems. The key point here is in stabilizing non-neutral conditions, as realized in CREM by the combined X-ray plus eFG input signals. *In vivo*, an analogous situation can be dictated *via* pH changes, such that capturing a small molecule may be favored within a given pH range, whereas at a different pH range, the release of this molecule is favored. The fact that the specific Trp214 molecular site can dictate the effective affinity of the entire macromolecule may therefore be exploited in both bio-systems and purely solid-state device configurations.

7.2. Mutual dependencies between structure and electrical characteristics

Evidence for additional complexity in the analysis of BSA-SAM properties was revealed by inspecting the fine XPS-CREM

details in an extended set of samples, using additional dopant molecules.[117,120,126] It should be noted first that doping of nano-objects is different from the classical doping of semiconductors. For nanoparticles, or medium-sized proteins like BSA, the attachment of dopants *via* targeting each particle, sometimes even a specific molecular site, involves dopant densities that are extremely high at a distribution that is far from being random. With C_{60}-BSA, this ideal feature was practically achieved. Similarly, additional small molecules appeared to successfully bind to BSA, however not necessarily to a single specific site. While electrical characteristics could be derived for all those systems, it turned out that their self-assembly on gold, conformation-wise and even composition-wise, varied considerably with the dopant type.

The evaluation of these effects relied on observables relatively easy to be followed and XPS-quantified. Most interesting results were obtained from the oxygen content and the degree of substrate coverage, namely, the density of SAM packaging. These two were found to be correlated, indicating that BSA dehydration was dopant-dependent and, relatedly, the surface coverage was affected too. In particular, the amount of water molecules remaining in the BSA-based layer was estimated to vary, depending on the doping type, from 0.7 to 2.0 water molecules per N atom. The lowest content was found in un-doped BSA. While exhibiting very significant dehydration upon assembly on gold, the bare BSA was suggested to also undergo conformational changes that effectively formed steric intermixing between 'molecular branches' of neighboring molecules, presumably *via* interactions with active SH groups. Thus, compact assembly with minute intermolecular spaces was realized, involving changes in shape of the individual molecules. On the other hand, in the doped samples, intramolecular interactions appeared to be stronger, such that dehydration was suppressed. Possibly, dopant molecules would preferably bind to peripheral sites of the BSA and thus prevent the SH groups from forming inter-molecular linkages. Thus, conformational changes were more limited and the spaces left between neighboring molecules in the SAM phase were more pronounced, similar in a way to the assembly of rigid particles. The detailed analysis can be found in the original paper and will not be described here.[120] Instead, some of the related electrical results are discussed.

Fig. 15 presents the representative *V*–*V* and *I*–*V* curves of doped and un-doped BSA-SAMs. Here it is the grid bias of the eFG that was varied, while the sample bias was kept fixed; an experiment essentially similar to those described above with

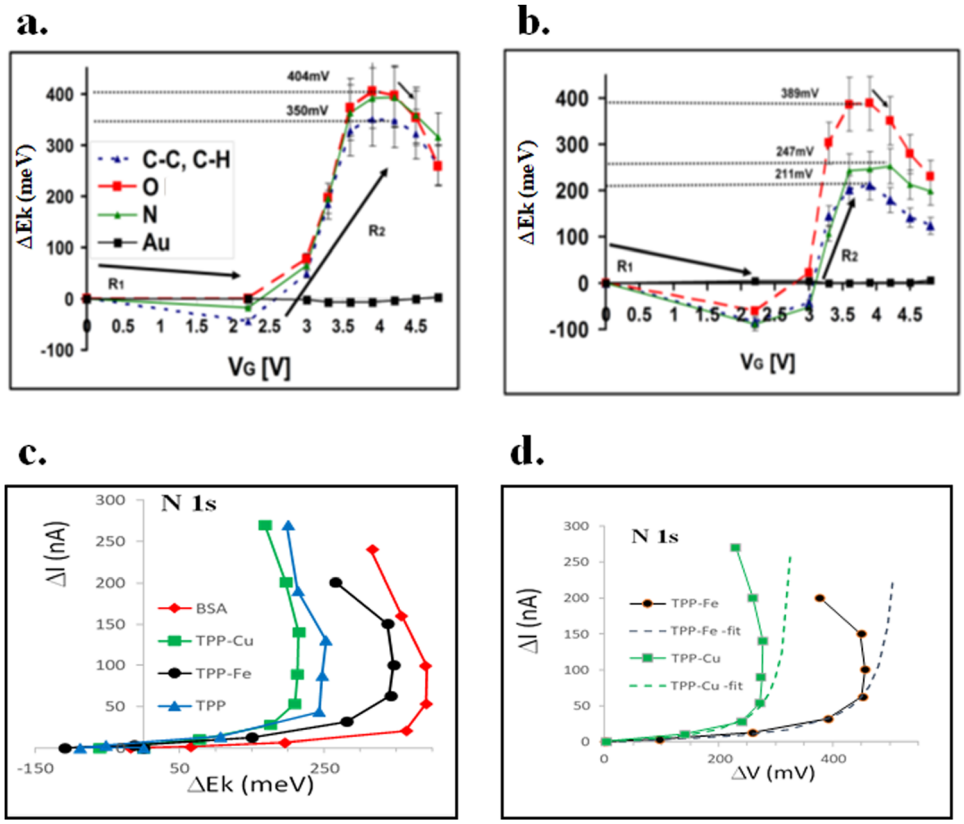

Fig. 15 TPP-based doping in BSA: early stages in the CREM element-specific *V*–*V* and *I*–*V* scans. The ΔE_k–V_G curves in un-doped (a) and PPT-doped (b) BSA exhibit degradation in samples' dielectric integrity under high current values (note the pronounced differences between samples for the *C* and *N* curves). (c) N-derived ΔI–ΔE_k curves of various doping types, demonstrating considerable differences in the potentials emerging under identical eFG parameters. (d) Two representative ΔI–ΔV curves with their theoretical (damage free) fit. ΔV in panel (d) refers to the eFG-related component in ΔE_k. All measurements were obtained under a step-wise increase in the eFG grid bias, V_G. Measurements sequence is indicated in panels (a) and (b) by arrows. Panels (a) and (b) were adapted from ref. 120.

fixed eFG parameters and varied sample bias. To start with, the reader is referred to the common shape of the *V–V* (also *I–V*) curves. According to the model described above (eqn 5), the maximal potential that these samples could gain, denoted here as ΔV_M, should express full occupancy of the charge traps, which is a valuable piece of information. Unfortunately, however, it was found that layer degradation under elevated fields prevented the experiment from reaching this limit and, in practice, the critical field at which these layers lost their electrical integrity was the actual feature probed. Fig. 15c demonstrates differences between the different dopants and Fig. 15d presents two curves with their theoretical fit, based on eqn 5, which clarify the loss of electrical integrity under high fields.

A more reliable feature of interest could be derived from the low-*V* limit of the *I–V* curves. The slope of the curve at that limit is given by *b*/*a*; a ratio that expresses competition between trapping and de-trapping efficiencies at the electron traps (see eqn (5)). Table 4 presents the corresponding slope values. In spite of the limited accuracy achieved in the derivation of $\Delta I/\Delta V$ slopes (Fig. 15c and d), the general trend and major result of a factor of about two between the extreme cases were both significant. Differences between samples were assigned mainly to discharging efficiencies, *b*. Expectedly, discharge *via* peripheral routes, along the outer surface of each BSA molecule, would be enhanced upon increased separation between neighboring molecules. It may also gain efficiency *via* hopping sites offered by the OH or water molecules. This way or another, the un-doped BSA presents an overlayer of lower conductivity that is strongly correlated with the morphology of the layer.

Complementary input in this matter is provided by differences observed between the elemental *V–V* curves. Fig. 15a and b present such curves for two BSA SAMs: un-doped and a doped variant. In spite of their common shape, differences are seen in each panel between the O and N curves (also C). The maximal voltage, ΔV_M, of the O-curves appears to reach larger amplitudes in all samples. However, the difference between O and N is sample dependent. Interestingly, this difference was rather small for un-doped BSA, the sample in which dehydration was maximal and, in contrast, it was maximal for the TPP doping, where dehydration was minimal. The values of ΔV_M are listed in Table 4. Negative correlation is seen, such that the same sorting-like order applies, just opposite in sign, matching also the ordering in dehydration magnitudes (note that NAP-CREM could be useful in this matter, provided that NAP-XPS is instrumentally available). The latter observation points to the role of water molecules and/or OH groups as electron traps in the BSA-based monolayers, expressed by locally increased electron densities.

Supported by additional characterization methods that were exploited in the original papers, rich information was produced consistently within the XPS analysis chamber. The advantage of conducting a multi-facet experiment and thus reduce the number of unknowns in each of its measurements was proven invaluable. Altogether, these results prove that the protein-based transistor device and its operation involve complex inter-relationships between structure, composition and electrical characteristics, all being mutually dependent. The CREM-XPS combination proposed, here again, a general notable advantage, allowing for the direct and joint detection of various characteristics that were inseparable in the protein-based device.

Finally, noting that the BSA study included contact-based electrical measurements in the MolVeT device, a valuable reference was proposed for the CREM-derived data. By way of comparison, both consistency between the probes and reliability of each could be verified. At the same time, fundamental and practical differences also became clearer, giving rise to data complementarity, such as the identification of selective charge trapping and its correlation with transport efficiencies. In a transistor device, one can use the gate electrode to dictate selective hole or electron injection and, also, control the effective energy of the injected charge, similar in a way to CREM. However, the CREM 'top-contact-free' configuration opens accessibility to valuable inner details. In particular, the ability to *in situ* construct sample's band diagram and to directly read potentials at chemically defined addresses, other than at an external electrode, proposes advantages of particular importance, even more so when organic molecules are intentionally incorporated at the core of the electrical device.

Table 4 Trends in doped BSA samples, as reflected by elemental (N and O) CREM data, ΔV_M and the *b*/*a* ratio. A decrease in ΔV_M correlates with an increasing *b*/*a* ratio. The experimental error in ΔV_M values is ±20 mV. The relative error in *b*/*a* ratios was estimated to be about 20%. Adapted from ref. 120

Sample	N − ΔV_M (mV)	O − ΔV_M (mV)	N − *b*/*a*	O − *b*/*a*
Un-doped	390	405	8	10
TPP-Fe	340	390	15	13
TPP-Cu	215	345	16	19
TPP	245	390	22	18

8. Ion diffusion in pectin

In the context of analytical chemistry, natural materials propose strategies for meticulous control over macro-scale physical performance.[127,128] This is frequently attained while valorizing properties of the building blocks such as to get a desired functionality of the emerging composite. One of the abundant examples is the interaction between polysaccharides and proteins. The former is known as a 'stabilizer' of proteins. Often, *via* such interactions, multifunctional performance is achieved, including improved protein thermal stability,[129,130] increased hydration in polysaccharides,[131] variable electrical conductivity and further diverse biological functions. Specifically, the electrical conduction in these composites was found to consist of mixed ionic and protonic conduction mechanisms, therefore presenting intriguing aspects for XPS-based analyses.

In a recent work by Rosenberg *et.al.*,[6] mixtures of the thermally sensitive and conductive pectin polysaccharide with

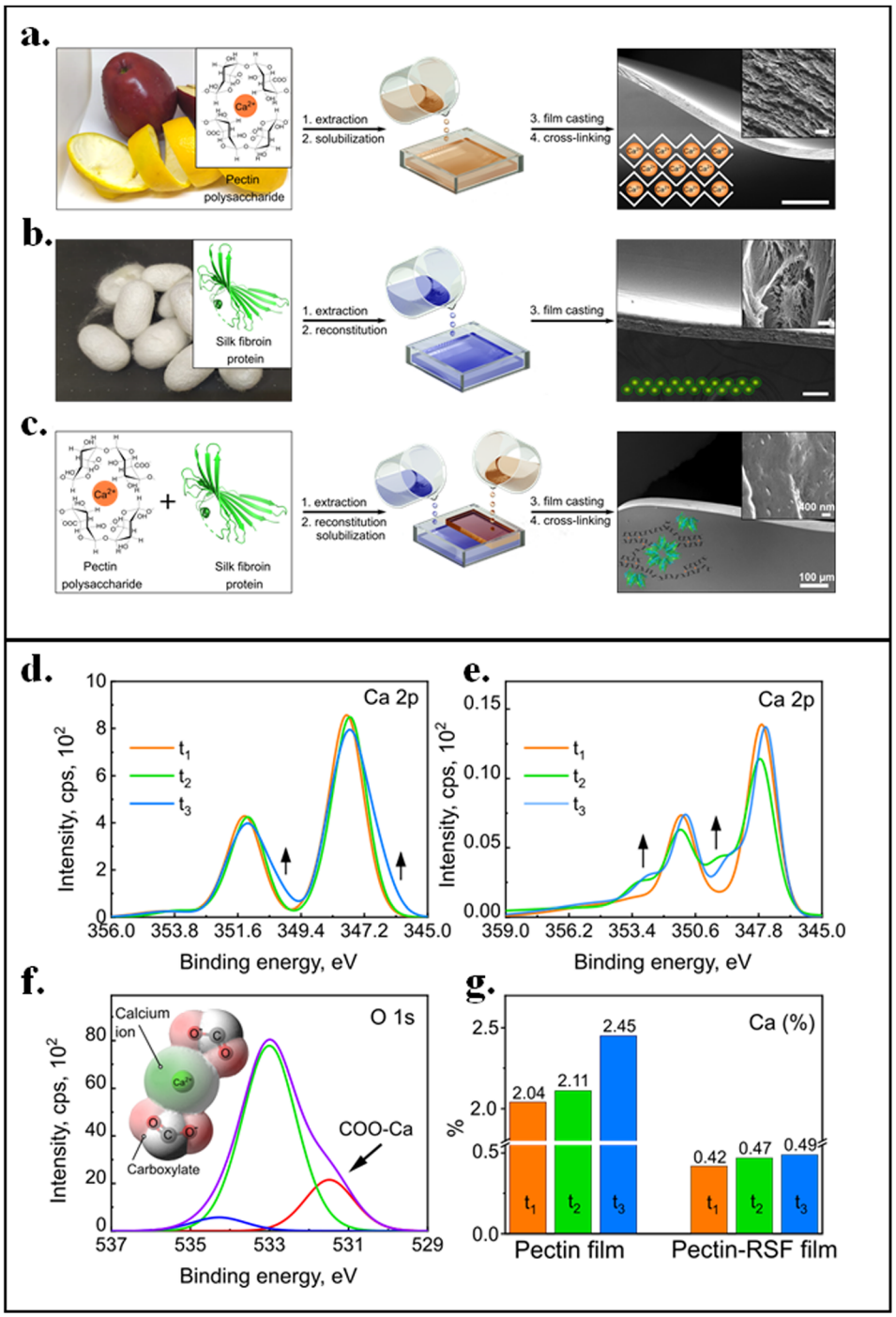

Fig. 16 Ca-Diffusion in pectin. (a–c) Process of material extraction schematically shown for (a) pectin polysaccharide, extracted from citrus fruits, (b) fibroin, extracted from silkworm cocoons, and (c) their mixture. Images of typical resultant structures are shown on the right. (d–g) XPS of the Ca 2p line of (d) pure pectin and (e) pectin-fibroin mixture, and (f) the O 1s line of pure pectin. Arrows in panels d and e indicate the emerging changes in Ca line-shape. The carboxylate O-component of eggboxes that bind Ca ions is indicated in panel f. The exposure times in panels (d) and (e) were: $t_1 \approx 12$ min, $t_2 \approx 60$ min, $t_3 \approx 120$ min, corresponding to an X-ray source power of 75 W, an eFG filament current of 1.9 A and a grid voltage of $V_G = 5$ V. (g) Summary of Ca atomic concentrations at the times presented in panels (d) and (e).

the mechanically strong silk fibroin have been studied, as part of a more general research on multifunctional composite materials.[132] Fig. 16 (top panel) presents schematically the means used at the Weizmann Institute for extracting pectin from citrus fruits (Fig. 16a), fibroin from silkworm cocoons (Fig. 16b) and preparation of their mixture (Fig. 16c). As part of this project, the mechanism of electrical conductivity, which is known to be dominated by Ca^+ diffusion, was investigated in

pure pectin and in its composite with fibroin, tested under varied thermal and humidity conditions, and, complementarily, by controlled surface charging in XPS.

Pectins are plant polysaccharide molecules playing a unique multifunctional role in nature. Pectin carbohydrates can differ from each other, and with structural variations comes the diversity in supramolecular organization and in physical properties. Pectin is a polymer with a linear structure in which a few hundreds to thousands galacturonic acid monomer units are linked *via* an α-(1 → 4)-glycosidic bond, forming a backbone. The average molecular weight of pectin ranges between ∼50 and ∼150 kDa. The backbone of pectin molecules is substituted at certain regions with α-(1 → 2) rhamnopyranose units, from which side chains of galactose, mannose and xylose, may occur. The linearity of the pectin, especially its capability to form nanoscale fibers both in the form of gel and in the form of solid, make this material nearly perfect for supporting the structure of plant cells.

A couple of notable pectin properties that originate from its structural characteristics are the ability to hold water molecules and to conduct electrical current, which is, in turn, highly sensitive to temperature changes. Upon self-assembly, pectin biopolymers can form an ''eggbox''-like structure (left inset to Fig. 16a), aligning negatively charged carboxylate groups in the center of this supramolecular organization. Fig. 16a (right inset) shows a 2D arrangement of such units, forming planes of cavities that are occupied by Ca ions. Indicated in Fig. 16f, the ''eggbox''-related oxygen component in the XPS O 1s line is resolved. Such an arrangement of pectin enables a relatively easy migration of the Ca^{2+} ions along the eggbox chains, which results in electrical current. A variety of experiments have yielded supporting evidence for the realization of ionic conduction in this system.[133,134] The electric current was shown to increase significantly under increased humidity, being assisted by trapped water molecules in the host structure. The level of hydration was further affected by the temperature changes and, thus, the ion conduction efficiency varied. Effectively, strong thermo-responsive conductivity is realized, to which one can add the dependence on structural degrees of freedom, such as to achieve fine-tuning of capabilities.

To be distinguished from pectin, fibroins demonstrate other valuable properties, such as shear and thermal sensitivity, proposing a remarkable capability to re-organize into highly ordered complexes, assembled into the crystalline β-sheet units mainly *via* H-bond interactions (also see the next section). The production of fibroin in arachnids and insects is by itself a very interesting phenomenon, going through transitions between liquid and solid phases *via* spinning (and elongational flow) of liquid crystal pulp into the crystalline fibers that, as a final result, present unique mechanical properties.[132] In general, at the micrometer scale, fibroins tend to self-assemble into functional amyloids, while environmental conditions such as pH, temperature, and concentrations affect the conformation of the secondary structures (β-sheets, random coil and α-helices) and, consequently, modify the physical macroscopic properties.

Practically, upon mixing pectin and fibroin, only a narrow range of relative concentrations (fibroin/pectin ratios of 3–5) yielded robust and homogeneously distributed mixtures. Lower fibroin/pectin ratios resulted in a global phase separation. In turn, all the successful mixtures exhibited short-range phase separations, on the scale of ∼50 nm. As a result, the role of domain interfaces became increasingly important, while yet, some of the individual properties of each constituent were expected to be preserved. In particular, protein is known to be a very good insulator and, as such, it was expected to enable partial control over conductivity in its solid-state solution with pectin.

Standard electrical measurements along films that were kept under controlled humidity, using solid-state electrodes at two sides of the film, were performed, showing remarkable sensitivity of pectin, as well as its mixture with fibroin, to humidity. Time dependencies and the role of additional parameters affecting the conductivity are presently under continued study. So far, in spite of the considerable amount of research supporting evidences by various techniques, differentiating between ionic currents and the ion-assisted electron currents has remained poorly answered.

However, an answer to the latter question was proposed by the XPS-based data. Fig. 16d and e show the XPS Ca 2p lines, recorded at different times of a long experiment, on a scale of a few hours, in which the sample was continuously exposed to the X-ray flux plus eFG electron flux, both kept under constant conditions. Besides slight evaporation of O-containing moieties (relative changes of 2–3%, see the original paper), a pronounced increase is noted in the Ca signal, about 20% in relative intensity, far above what one would expect from the evaporation/removal of surface species. Fig. 16g summarizes the related intensity changes. They are attributed to vertical Ca diffusion up to the top surface. A similar beam-induced process was already reported on, observing de-intercalation, *in situ* and during the XPS measurements, of alkaline metals out of transition metal dichalcogenides (TMDs).[135] Similar to the case shown here, diffusion of metal cations was induced by stabilizing a large amount of extra negative charges on the surface, which set a field that could drive the ion diffusion. In the present case, the diffusion process could be followed directly *via* the increase in Ca signal as a function of irradiation time and, importantly, also by the development of a component of reduced Ca, as indicated by the arrows in Fig. 16d.

To what extent such diffusion could proceed? Channels for a relatively easy diffusion of cations are indeed available in the pectin matrix and, in this respect, one may expect large amounts of bulk Ca to accumulate on the top surface. However, the Ca diffusion is known to be assisted by humidity, while the UHV environment dictates extremely low amounts, if at all, of residual water molecules within the host matrix and its surface. Therefore, the experimental result proves, first, that an electrical drive can indeed activate the diffusion of this cation. Second, it indicates that in the absence of water molecules, the process is self-limiting, presumably because of an opposing field created by 'emptied' cages that are left behind. Water

molecules, when available, can replace the Ca ions and fill those cages, such as to allow continuation of the diffusion process. It was therefore suggested that, on the sub nanometer scale, the presence of a water molecule in proximity to a Ca ion can reduce the energy barrier for the hopping process between neighboring cages. Further study is needed for detailed understanding of this mechanism. Yet, as an additional support, our *ex situ* electrical measurements have also encountered limited extents of the Ca-ion diffusion; a humidity-dependent feature whose quantitative evaluation under controlled conditions is still in progress.

When intermixed with fibroin, the process of ion diffusion is expected to be influenced by the fact that pectin is confined to mesoscale islands. For XPS, an island thickness of 50 nm is already enough for vertical diffusions to be of significant impact on signal intensities. Our experimental results show indeed a relative increase in Ca intensity (see Fig. 16g) similar to the one of pure pectin (for which the absolute Ca intensities were much larger indeed). This fact suggests that, locally, the diffusion efficiency is similar to the one in pure pectin and the quasi-2D structure of pectin is retained in the mixed phase. However, in view of final oxidation states, the diffused Ca in the mixed structure does not become more reduced. On the contrary, a shoulder of more oxidized Ca appears (shown by arrows in Fig. 16e), slightly above the experimental error level. The oxidized-Ca component is believed to result from reactions occurring at domain interfaces with the fibroin. Namely, the field created by the eFG is well established, but the released Ca ions can interact with oxygen, possibly water molecules incubated at interfacial domains, and thus become 'protected' from free electrons that arrive from the eFG.

In particular, the latter experiment exemplifies a trivial capability of XPS: its standard elemental composition analysis, with which vertical diffusion can be identified. It is the electrical drive that was added in these experiments by means of the eFG, a low-energy electron flux supplied from an external source. In this respect, the eFG operates similarly to a decent electrical contact, while yet allowing direct inspection of the composition at the active surface.

9. XPS of hydrogen bonds in peptide-based assemblies

Protein self-assembly[136] is a highly non-linear process governed by structural transformation from native protein folds into supramolecular amyloid structures rich in β-sheets. Traditionally, a variety of external stimuli affect the transition between a dispersed protein solution and a solid protein state, leading to diverse micro-scale structural conformations and macro-scale physical properties. Interestingly, this self-assembly process gained popularity upon the emerging design of biomaterials with programmable properties.[4,137–141]

A vital role in biological molecules is played by hydrogen bonds (H-bonds). For example, the formation of intra-chain hydrogen bonds in proteins can stabilize chiral structures, whereas inter-chain H-bonds frequently lead to the formation of fibers and β-sheets. These structural variations lead to markedly different properties, with significant impacts on biological processes and, potentially, on future materials sciences. A question is therefore raised about the capability of electron spectroscopies to characterize these H-bonds. As already mentioned, electron microscopy (EM) and electron spectroscopy are commonly considered blind to hydrogen, with one exception: the low beam-energy configuration of high-resolution electron energy loss spectroscopy (HREELS) that, unfortunately, proposes very poor imaging capabilities.[142] Recently, an instrumental development in scanning transmission electron microscopy (STEM), TEM- and STEM-EELS, has enabled significant improvements in energy resolution,[143] which open accessibility to the IR spectral regime, including that of hydrogen vibrations. Thus, hydrogen signals can be recorded nowadays from small (laterally sub-nanometer) spots, establishing a remarkably powerful electron spectromicroscopy of hydrogen.

Beam damage in such experiments is of mandatory concern, requiring sample freezing techniques. However, as an alternative approach, it was recently shown that beam damage in STEM-EELS can be practically eliminated by using the non-touching (aloof) scattering configuration,[144–146] where the e-beam is directed along xy positions that are close, however having no geometric intersection with the studied object. This EELS configuration essentially probes the near-field plasmonics, with a 'tip' (the e-beam) that is only a couple of angstroms wide.[147,148] Extension of this EELS feature was demonstrated on natural guanine crystals,[149] see Fig. 17. It was shown that hydrogen vibrations could be detected with no need in freezing or fixation and, practically, with no sample damage. The parameter of beam-sample distance sets in these experiments a cutoff on the energy range available for excitation of the sample. By choosing relatively large distances, $\geq$30 nm in that case, the vibrational spectrum could indeed be collected at practically zero damage formation, in spite of the high e-flux used and the fact that the sample was held at room temperature. Fig. 17b shows two leading signals in such a spectrum. Their stability on a scale of many minutes is shown in Fig. 17c. In contrast, once the beam-sample distance was decreased such as to allow higher excitation energies, above *e.g.* the sample's ionization threshold, the damage evolution was accelerated pronouncedly, as shown in Fig. 17d. In a different terminology, at smaller distances, virtual photons of higher energies are exchanged between the beam and the sample. Still, sample degradation at small beam-sample distances was much slower than in the standard EELS configuration, in which the beam was traversing the studied object and high-impact scattering events were stimulated.

It should be noted that, somewhat similar to the EM experiments, the scanning probe microscopy (SPM) technique, combined with spectroscopic capabilities, such as nano-IR,[150] has become very useful in probing vibrational spectra from small selected objects. Their lateral resolution is not as good as that in EM, but experiments can be performed in an ambient

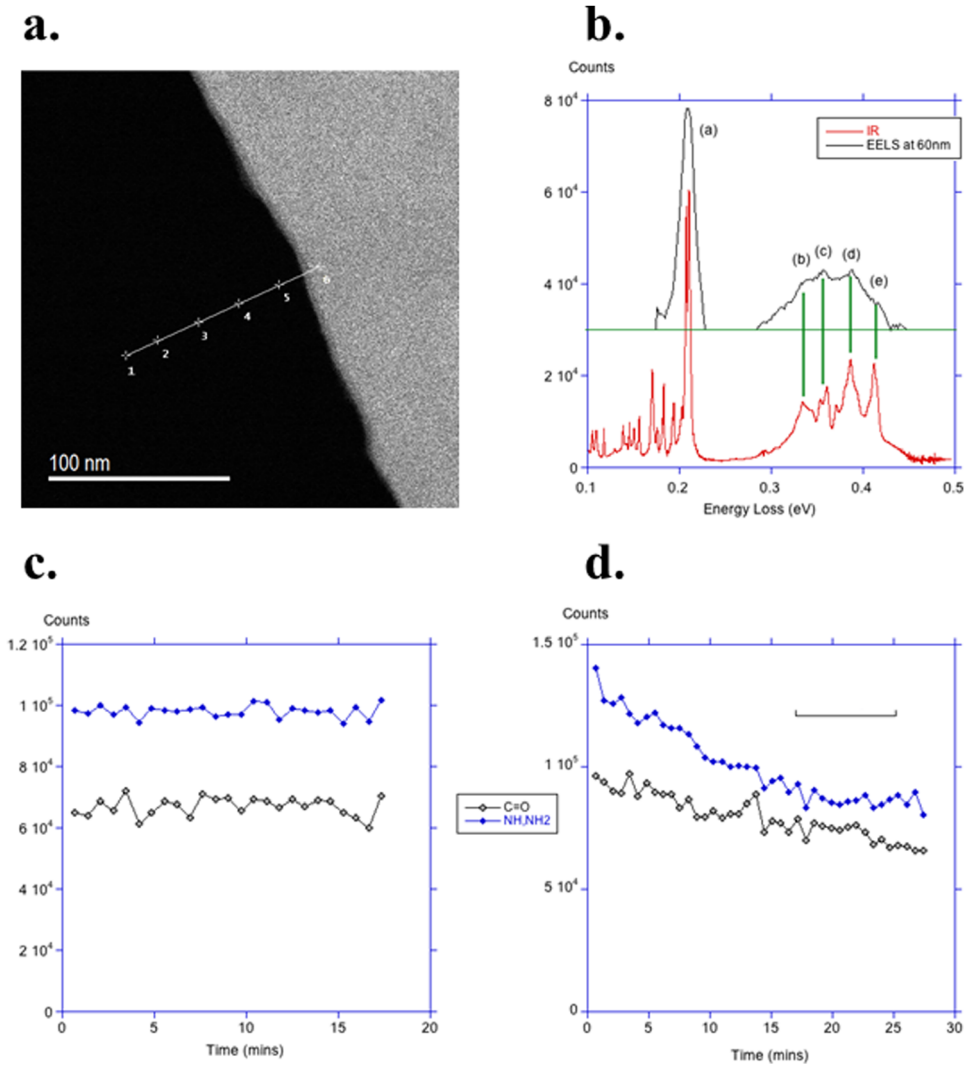

Fig. 17 Non-damaging STEM-EELS of guanine. (a) STEM image of the edge of a guanine crystal. Positions are marked through which the e-beam was directed for the near-field EELS measurements. (b) The IR spectral regime of guanine as obtained in solution by optical IR (red) and in vacuum by the EELS probe (black). (c) Time dependence of EELS intensities for a beam-sample distance of 30 nm, showing practically no damage in the C═O (black) and N–H (blue) vibrations. (d) Same as (c), measured at a beam-sample distance of 10 nm, showing slow degradation. Adapted from ref. 149.

atmosphere following easier sample preparation protocols. Studying the assembly of proteins by nano-IR is presently a work in progress by the Weizmann group[132] and collaborators, allowing, for example, an easy differentiation between micelles, fibers of different shapes, *etc.*

Independently, an interesting opportunity for resolving related features at the molecular scale can, in principle, be obtained by XPS because information on vibrational excitations is expected to appear as satellites to elemental lines. Thus, a novel probe based on chemical addresses, similar in a way to the CREM data, may be established. However, as of today's instrumentation, XPS is incapable of resolving such vibrational signals. Therefore, combined with its inability[151] to directly quantify hydrogen contents, XPS derivation of H-bond characteristics is far from being trivial. Yet, in a recent work by Aggarwal *et al.*,[152] it was shown that such information can be inferred from signals emitted from neighboring atoms. This paper further demonstrates how the amyloidogenic nature of proteins can be guided and controlled upon intervening the H-bond network formation and other competing protein assembly factors. Pre-designed modifications of the molecular interactions thus offered useful triggering means of amyloidogenic fibrillation and a rational for 3D organization into high macroscale hierarchies, demonstrating different morphologies and structural configurations.

A set of seven peptide chains with synthetically modified backbones was used, such as to introduce steric and chemical constraints and, thus, influence the self-assembly process, its kinetics and the final shapes formed. Fig. 18a depicts the central idea of amino-acid substitution, from aliphatic to aromatic, in the peptide sequence. The full set of peptides with their attached side groups is shown in Fig. 18b, next to the resulting morphologies, as obtained by atomic force microscopy (AFM). It is noteworthy that the pronounced differences

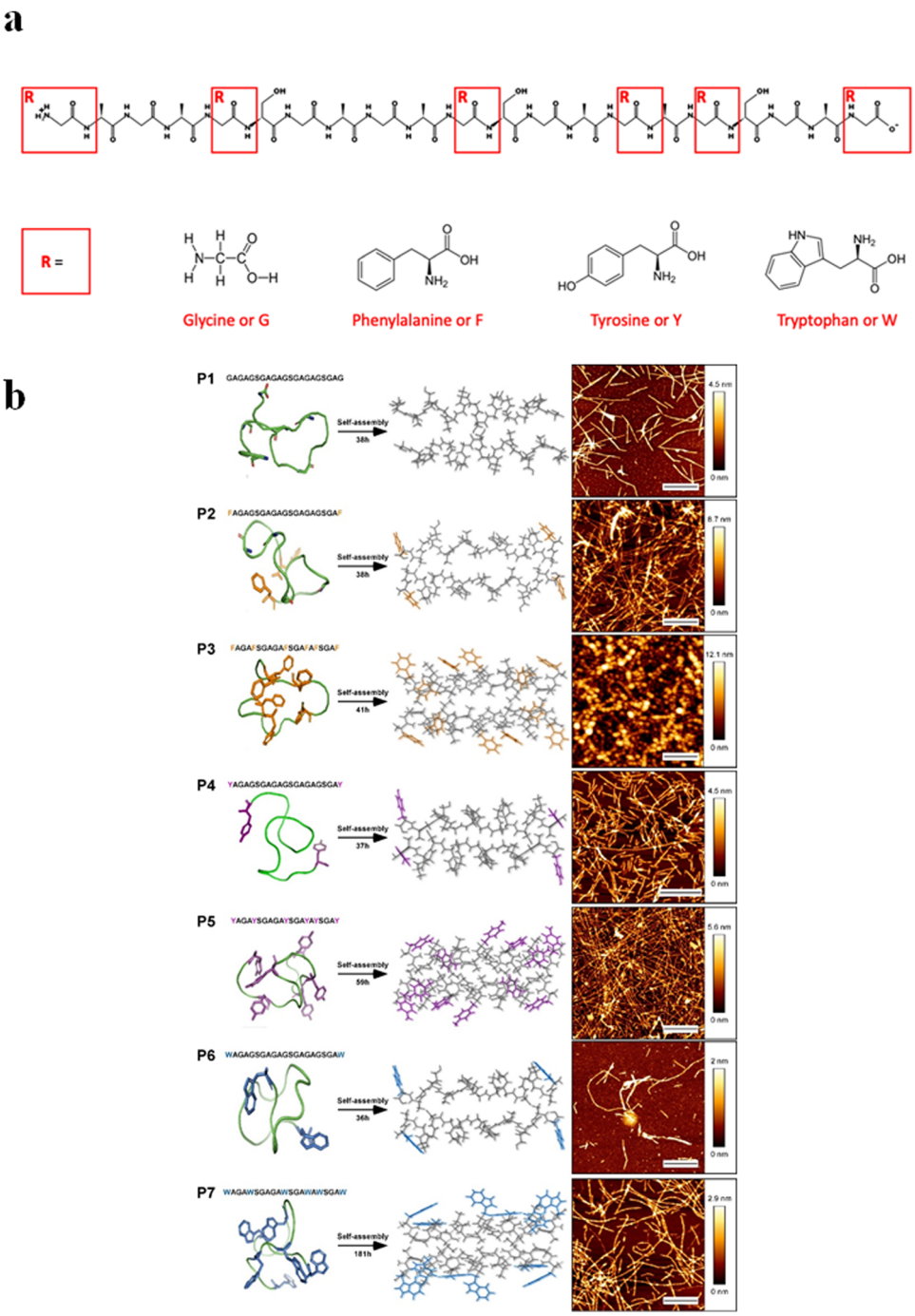

Fig. 18 Synthesized peptide backbones. (a) Illustration of the methodology for amino-acid substitution, from aliphatic to aromatic, in the peptide sequence. (b) Full set of peptides with their attached side-groups and the resulting morphologies, as obtained by atomic force microscopy (AFM). Note the pronounced differences in macro morphologies. Mechanical differences were also identified, not shown. Taken from ref. 152.

in macro morphologies, P3 and P6, which are rich in hydrophobic groups and hence suppress H-bond formation, are dominated by spherical structures, in contrast to the fibrillary structures of the other peptide backbones. Differences in the length and elasticity of the fibers were also identified and quantified in the original paper.

Technically, the XPS quantification of H-bonds *via* neighboring atoms, as mentioned above, encountered a serious difficulty due to differential charging effects. Peptides are known to be highly insulating, formed in non-uniform thicknesses, sometimes with morphology that dictates a non-uniform effective flux of the X-ray beam, *via* shadowing for example, as well as of the eFG electrons. This difficulty was further amplified because spectral shoulders next to intensive signals were at the core of the analysis, while in general such shoulders, even under slight distortions, tend to suffer

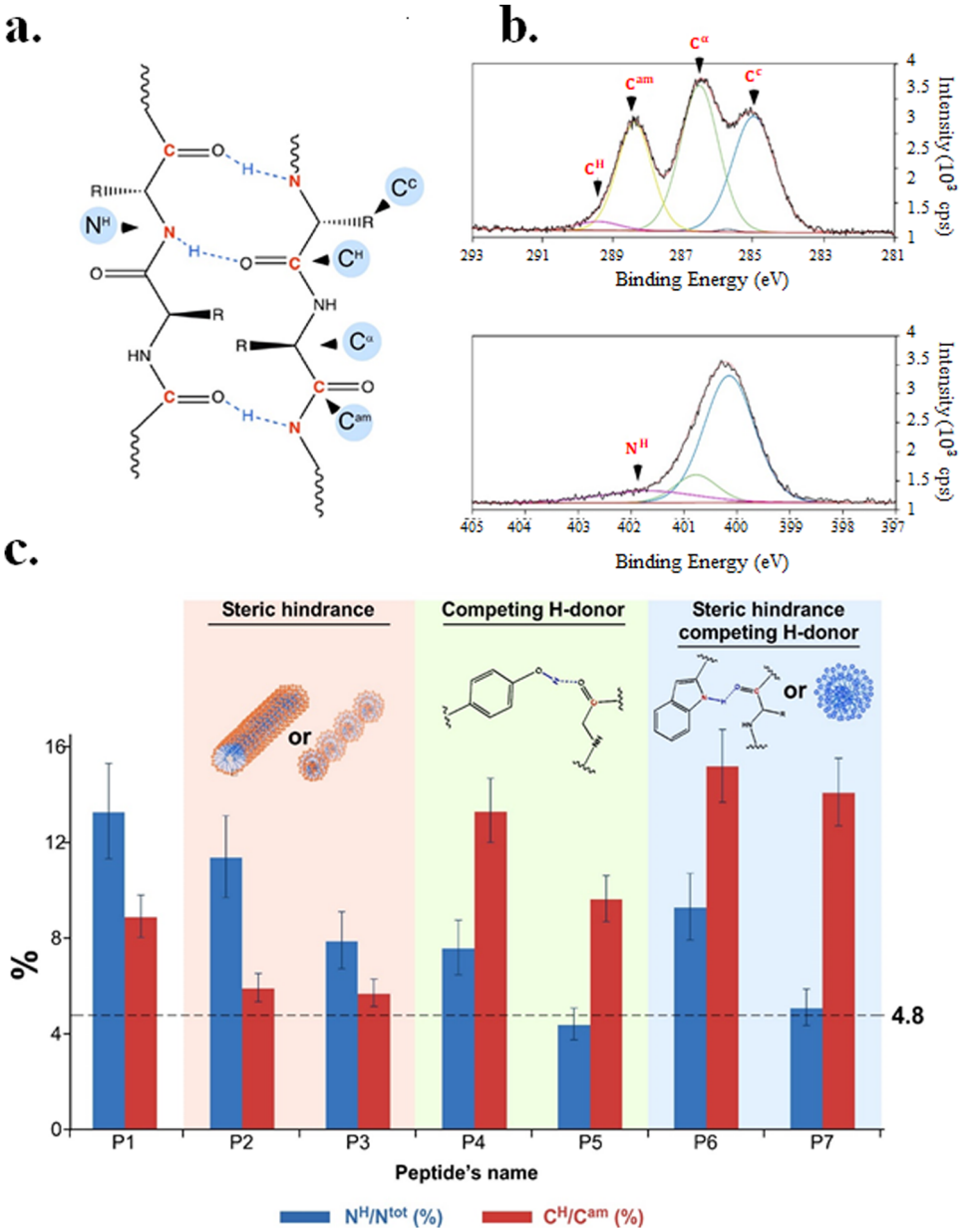

Fig. 19 H-bond evaluation in synthetically modified peptides. (a) Illustration of H-bonds formed between amide groups of neighboring chains. Selected atomic sites are indicated, corresponding to peaks indicated in panel b. Note that H-bond neighbors are labeled as C^H and N^H. (b) XPS C 1s (top) and N 1s (bottom) lines, as recorded from P1, with indications of selected elemental components. (c) Summary of the XPS-derived H-bond amounts, each normalized to the amount of total amide groups, as derived from the C (red) and N (blue) signals. The dashed line in panel c stands for the theoretical amount of chain end-groups, to which all histogram values should refer. Adapted from ref. 152.

relatively large changes. Therefore, top-quality elimination of the differential charging effects became essential for any detailed line-shape analysis in this project. Answers came upon the application of dedicated experimental protocols that included scans with extremely low X-ray flux, prior to the main part of these experiments, as well as scans under varied charging conditions, such that the evolution of spectral distortions could be inspected in detail.[70]

Expectedly, upon H-bond formation, the neighboring N and C atoms, on both sides of the O–H bond, should become more oxidized; namely, lose some of their electron density. Fig. 19a illustrates the formation of H-bonds between two amide groups, and Fig. 19b presents the measured C 1s and N 1s lines of P1, for which H-bond-related shoulders are indicated by arrows. The corresponding atomic concentrations are given in Table 5, and the H-bond related amounts are summarized in Fig. 19c, normalized to the total amount of amide groups. For the latter, a common value of 4.8% should be subtracted due to overlapping signals originating from the end-groups of these chains, as indicated by a dotted line in Fig. 19c. Clear differences are seen between the various peptide backbones, indicating that the side groups tailored to these chains did indeed

Table 5 Compositional evaluation of peptide characteristic signals, given as atomic ratios in the set of modified backbones. Theoretical (ideal) values are provided for comparison. Taken from ref. 152

	N/C^{am}		C^{α}/C^{am}		C^{C}/C^{am}		O/C^{am}	
	Theory	Exp.	Theory	Exp.	Theory	Exp.	Theory	Exp.
P1	1	0.96	1.142	1.315	0.333	1.215	1.19	1.5
P2	1	0.99	1.142	1.235	1	1.8	1.19	1.52
P3	1	1.015	1.142	1.54	1	3.21	1.19	1.195
P4	1	1.05	1.238	1.49	0.904	2.17	1.19	2.98
P5	1	1.015	1.428	1.935	2.047	3.07	1.268	2.13
P6	1.095	1.035	1.142	1.56	1.19	2.325	1.476	2.08
P7	1.285	1.245	1.142	1.825	2.904	4.185	1.19	2.345

affect the ability to form H-bonds upon self-assembly, in agreement with the AFM images in Fig. 18. Consequently, both macro-scale shapes and material properties exhibit prominent differences that emerge all from the molecular level energetics, the steric restrictions introduced by the side groups and the competing bond formation with solvent molecules. Having those taken into account, the various independent pieces of experimental results on assembly kinetics and the final structure obtained for each of the studied backbones could all be explained consistently.

It should be stressed that the evaluation of H-bonds in this study remains, essentially, in the domain of chemical analysis. However, its reliability strongly depends on the CREM-based elimination of charging artifacts. Finally, an attempt to inspect the H-bonds in chiral molecules, namely intra-chain H-bonds, in a similar way has been conducted recently.[153] The results were limited in the sense that the identification of spectral shoulders at the C 1s and N 1s core lines was indeed successful; however, the related spectra did not enable sufficient sensitivity to differences that might allow differentiation between the chiral-type (alpha) and the fiber-type (beta) H-bonds. The only clear difference observed in this respect regarded the stability of these bonds under X-ray irradiation, which appeared to be much poorer for the chiral molecules.

10. Summary

A partial review of XPS applications to studies of macro and small organic molecules was attempted, describing the 'promise and challenges' typical of this field. In its main message, the review describes the advantages proposed by harvesting electrical information which is inherent to electron spectroscopy tools, in combination with the chemical information of 'standard' XPS. Three categories of added values opened by the combined CREM-XPS experiment have been noted. First, the standard chemical analysis can frequently gain critical assistance from the electrical data *via*, for example, the elimination of charging artifacts, the improved identification of beam-induced damage and the availability of independent depth profiling for the attenuation factors, each of which proposes marked improvements in the basic compositional analysis. Second, the access to electrical information opens a whole dimension of properties that can be studied within the XPS chamber and, importantly, when extracted together with the chemical data, *in situ* and under the very same experimental configuration, one also avoids un-necessary unknowns that typically arise in separated experiments, toward a comprehensive and easier interpretation of data. Third, it turns out that some of the CREM features provide information that is unique as compared to any standard electrical tool, thanks to the absence of top electrodes, the availability of atomic addresses and the enhanced sensitivity to hot-charge characteristics.

All these features gain particular importance due to a variety of spectro-microscopy challenges typically encountered in studies of soft matter and bio-molecules. Rich inter-relationships were revealed, even for relatively simple systems, between the electrical characteristics, the structural defects, the compositional variations and more. The cases described here, starting from small molecules and ending in large proteins, exhibit such mutual relationships and emphasize the considerable complexity to be encountered in any related research. Evolutionary solutions that are found in molecular scale biomechanisms, as well as the promising utilization of similar designs in artificial devices, both present demands that exemplify added values of the CREM-XPS technique. It is therefore believed that this field of research can potentially be expanded and elaborately developed to provide a template for advanced characterization strategies in future studies of bio- and nature-inspired systems.

Conflicts of interest

There are no conflicts to declare.

Data availability

All data included in this review have been published and/or are available upon request.

Acknowledgements

We thank Prof. Samuel Safran and Prof. Itamar Procaccia for helpful discussions on aging and Dr Mark Iron for providing DFT-based calculations of sub-molecular potentials in iodine- and chlorine-terminated molecules. H. C. acknowledges the financial support by the Israeli Science Foundation, project no. 604, and The Helen and Martin Kimmel Center for Molecular Design. U.S. acknowledges financial support from NATO (G6194), Human Frontiers Scientific Program- HFSP (**https://doi.org/10.52044/HFSP.RGP0202024.pc.gr.194172**). U.S. also thanks the Perlman family for funding the Shimanovich Lab at the Weizmann Institute of Science.

References

1 N. Amdursky, M. Molotskii, E. Gazit and G. Rosenman, Elementary Building Blocks of Self-Assembled Peptide

Nanotubes, *J. Am. Chem. Soc.*, 2010, **132**(44), 15632–15636. Available from: https://pubs.acs.org/doi/abs/10.1021/ja104373e.
2 T. P. J. Knowles and M. J. Buehler, Nanomechanics of functional and pathological amyloid materials, *Nat. Nanotechnol.*, 2011, **6**(8), 469–479. Available from: https://www.nature.com/articles/nnano.2011.102.
3 T. P. J. Knowles, T. W. Oppenheim, A. K. Buell, D. Y. Chirgadze and M. E. Welland, Nanostructured films from hierarchical self-assembly of amyloidogenic proteins, *Nat. Nanotechnol.*, 2010, **5**(3), 204–207. Available from: https://www.nature.com/articles/nnano.2010.26.
4 U. Shimanovich, G. J. L. Bernardes, T. P. J. Knowles and A. Cavaco-Paulo, Protein micro- and nano-capsules for biomedical applications, *Chem. Soc. Rev.*, 2014, **43**(5), 1361–1371.
5 E. Abraham, D. E. Weber, S. Sharon, S. Lapidot and O. Shoseyov, Multifunctional Cellulosic Scaffolds from Modified Cellulose Nanocrystals, *ACS Appl Mater Interfaces.*, 2017, **9**(3), 2010–2015. Available from: https://pubs.acs.org/doi/abs/10.1021/acsami.6b13528.
6 A. Rosenberg, A. Solomonov, H. Cohen, D. Eliaz, I. Kellersztein and O. Brookstein, *et al.*, From Basic Principles of Protein-Polysaccharide Association to the Rational Design of Thermally Sensitive Materials, *ACS Appl. Mater. Interfaces*, 2024, **16**(7), 9210–9223.
7 A. Yonath, X-ray crystallography at the heart of life science, *Curr. Opin. Struct. Biol.*, 2011, **21**(5), 622–626.
8 T. Auerbach-Nevo, R. Zarivach, M. Peretz and A. Yonath, Reproducible growth of well diffracting ribosomal crystals, *Acta Cryst.*, 2005, **D61**, 713–719. Available from: https://scripts.iucr.org/cgi-bin/paper?ic5007.
9 R. Roy, S. Hohng and T. Ha, A practical guide to single-molecule FRET, *Nat. Methods*, 2008, **5**(6), 507–516.
10 M. Elbaum, S. Seifer, L. Houben, S. G. Wolf and P. Rez, Toward Compositional Contrast by Cryo-STEM, *Acc. Chem. Res.*, 2021, 423–428.
11 L. Houben, H. Weissman, S. G. Wolf and B. Rybtchinski, A mechanism of ferritin crystallization revealed by cryo-STEM tomography, *Nature*, 2020, **579**(7800), 540–543.
12 I. S. Tilinin, A. Jablonski and W. S. M. Werner, Quantitative surface analysis by Auger and x-ray photoelectron spectroscopy, *Prog. Surf. Sci.*, 1996, **52**(4), 193–335.
13 M. P. Seah and D. Briggs, *Practical Surface Analysis: Auger and X-ray Photoelectron Spectroscopy*, John Wiley & Sons, 1990.
14 G. Beamson, High Resolution XPS of Organic Polymers. *Science ESCA 300 Database*, 1992, Available from: https://ci.nii.ac.jp/naid/10003489274.
15 J. F. Watts and J. Wolstenholme, *An introduction to surface analysis by XPS and AES*, John Wiley & Sons, 2019.
16 C. J. Powell, Growth and trends in Auger-electron spectroscopy and x-ray photoelectron spectroscopy for surface analysis, *J. Vac. Sci. Technol., A*, 2003, **21**(5), S42. Available from: https://avs.scitation.org/doi/abs/10.1116/1.1599862.
17 C. J. Powell and A. Jablonski, The NIST electron effective-attenuation-length database, *J. Surf. Anal.*, 2002, **9**(3), 322–325.
18 *X-Ray Photoelectron Spectroscopy (XPS) Surface Analysis Technique*. Available from: https://www.phi.com/surface-analysis-techniques/xps-esca.html.
19 *Home - Scienta Omicron*. Available from: https://scientaomicron.com/en.
20 C. S. Fadley and S. Nemšák, Some future perspectives in soft- and hard- X-ray photoemission, *J. Electron Spectrosc. Relat. Phenom.*, 2014, **195**, 409–422.
21 W. Drube, Hard X-ray Photoelectron Spectroscopy, *Synchrotron Radiation News*, 2018, **31**(4), 2–3. Available from: https://www.tandfonline.com/doi/abs/10.1080/08940886.2018.1483647.
22 D. G. Castner and B. D. Ratner, Surface characterization of butyl methacrylate polymers by XPS and static SIMS, *Surf. Interface Anal.*, 1990, **15**(8), 479–486. Available from: https://onlinelibrary.wiley.com/doi/full/10.1002/sia.740150807.
23 A. G. Shard, Practical guides for x-ray photoelectron spectroscopy: Quantitative XPS, *J. Vac. Sci. Technol., A*, 2020, **38**(4), 041201. Available from: https://avs.scitation.org/doi/abs/10.1116/1.5141395.
24 M. A. Kelly, *Historical perspectives on charging issues in XPS*, Elsevier, 2010.
25 D. R. Baer, K. Artyushkova, H. Cohen, C. D. Easton, M. Engelhard and T. R. Gengenbach, *et al.*, XPS guide: Charge neutralization and binding energy referencing for insulating samples, *J. Vac. Sci. Technol., A*, 2020, **38**(3), 31204.
26 J. Cazaux, About the charge compensation of insulating samples in XPS, *J. Electron Spectrosc. Relat. Phenom.*, 2000, **113**(1), 15–33.
27 R. W. M. Chan, R. W. M. Kwok and W. M. Lau, Modified surface charge spectroscopy for the characterization of insulator/semiconductor structures, *J. Appl. Phys.*, 1996, **79**(7), 3635–3639.
28 T. L. Barr, Recent advances in x-ray photoelectron spectroscopy studies of oxides, *J. Vac. Sci. Technol., A*, 1991, **9**(3), 1793–1805.
29 R. W. M. Kwok, W. M. Lau, D. Landheer and S. Ingrey, Surface charge spectroscopy—A novel surface science technique for measuring surface state distributions on semiconductors, *J. Electron. Mater.*, 1993, **22**(9), 1141–1146.
30 I. Doron-Mor, A. Hatzor, A. Vaskevich, T. van der Boom-Moav, A. Shanzer and I. Rubinstein, *et al.*, Controlled surface charging as a depth-profiling probe for mesoscopic layers, *Nature*, 2000, **406**(6794), 382–385. Available from: https://www.nature.com/articles/35019025.
31 K. Shabtai, I. Rubinstein, S. R. Cohen and H. Cohen, High-Resolution Lateral Differentiation Using a Macroscopic Probe: XPS of Organic Monolayers on Composite Au−SiO_2 Surfaces, *J. Am. Chem. Soc.*, 2000, **122**(20), 4959–4962. Available from: https://pubs.acs.org/doi/abs/10.1021/ja993710h.
32 S. Suzer, Differential Charging in X-ray Photoelectron Spectroscopy: A Nuisance or a Useful Tool?, *Anal. Chem.*, 2003, **75**(24), 7026–7029. Available from: https://pubs.acs.org/doi/full/10.1021/ac034823t.

33 V. Artel, Q. Guo, H. Cohen, R. Gasper, A. Ramasubramaniam and F. Xia, *et al.*, Protective molecular passivation of black phosphorus, *npj 2D Mater. Appl.*, 2017, **1**(1), 1–5. Available from: **https://www.nature.com/articles/s41699-017-0004-8**.

34 A. Rozenblat, Y. Rosenwaks, L. Segev and H. Cohen, Electrical depth profiling in thin SiON layers, *Appl. Phys. Lett.*, 2009, **94**(5), 53116. Available from: **https://aip.scitation.org/doi/abs/10.1063/1.3073050**.

35 H. Cohen, Chemically resolved electrical measurements using x-ray photoelectron spectroscopy, *Appl. Phys. Lett.*, 2004, **85**(7), 1271–1273.

36 A. Givon, K. X. Steirer, E. Segre and H. Cohen, Doubly triggered conductance across thin zinc oxysulfide films, *Appl. Phys. Lett.*, 2018, **113**(9), 91602.

37 A. Givon, H. Piao, J. McMahon, G. Zorn and H. Cohen, Contactless derivation of inner fields in gate-oxide layers: SiO_2 on SiC, *Appl. Phys. Lett.*, 2015, **107**(17), 173101. Available from: **https://aip.scitation.org/doi/abs/10.1063/1.4934494**.

38 Y. Itzhaik, G. Hodes and H. Cohen, Band alignment and internal field mapping in solar cells, *J. Phys. Chem. Lett.*, 2011, **2**(22), 2872–2876.

39 A. Rozenblat, Y. Rosenwaks and H. Cohen, Hot-electron characteristics in chemically resolved electrical measurements of thin silica and SiON layers, *Appl. Phys. Lett.*, 2009, **94**(21), 213501.

40 N. Filip-Granit, M. E. van der Boom, R. Yerushalmi, A. Scherz, H. Cohen and N. Filip-Granit, *et al.*, Submolecular potential profiling across organic monolayers, *Nano Lett.*, 2006, **6**(12), 2848–2851. Available from: **https://pubs.acs.org/doi/full/10.1021/nl0620435**.

41 R. Yerushalmi, M. E. van der Boom and H. Cohen, Chemical site capacitance: Submolecular measurements and a model, *J. Phys. Chem. C*, 2007, **111**(37), 13652–13654.

42 H. Cohen, O. V. Zenkina, A. D. Shukla and M. E. van der Boom, Site affinity effects upon charge injection into siloxane-based monolayers, *J. Phys. Chem. B*, 2006, **110**(4), 1506–1508.

43 A. M. Moore and P. S. Weiss, Functional and spectroscopic measurements with scanning tunneling microscopy, *Annu. Rev. Anal. Chem.*, 2008, **1**, 857–882.

44 S. W. Wu, N. Ogawa and W. Ho, Atomic-Scale Coupling of Photons to Single-Molecule Junctions, *Science*, 2006, **312**(5778), 1362–1365. Available from: **https://www.science.org/doi/abs/10.1126/science.1124881**.

45 S. A. Claridge, J. J. Schwartz and P. S. Weiss, Electrons, Photons, and Force: Quantitative Single-Molecule Measurements from Physics to Biology, *ACS Nano.*, 2011, **5**(2), 693–729. Available from: **https://pubs.acs.org/doi/abs/10.1021/nn103298x**.

46 N. Nakatsuka, K.-A. Yang, J. M. Abendroth, K. M. Cheung, X. Xu and H. Yang, *et al.*, Aptamer–field-effect transistors overcome Debye length limitations for small-molecule sensing, *Science*, 2018, **362**(6412), 319–324. Available from: **https://www.science.org/doi/abs/10.1126/science.aao6750**.

47 P. G. Rouxhet and M. J. Genet, XPS analysis of bio-organic systems, *Surf. Interface Anal.*, 2011, **43**(12), 1453–1470. Available from: **https://onlinelibrary.wiley.com/doi/full/10.1002/sia.3831**.

48 D. R. Baer and M. H. Engelhard, XPS analysis of nanostructured materials and biological surfaces, *J. Electron Spectrosc. Relat. Phenom.*, 2010, **178–179**(C), 415–432.

49 D. R. Baer, M. H. Engelhard and A. S. Lea, Introduction to Surface Science Spectra data on electron and x-ray damage: Sample degradation during XPS and AES measurements, *Surf. Sci. Spectra.*, 2021, **10**(1), 47. Available from: **https://avs.scitation.org/doi/abs/10.1116/11.20040199**.

50 H. Tohma, Sample Surface Degradation of Organic Materials Caused during XPS Analysis, *J. Surf. Sci. Soc. Jpn.*, 2004, **25**(4), 192–197.

51 A. Shchukarev, Z. Gojkovic, C. Funk and M. Ramstedt, Cryo-XPS analysis reveals surface composition of microalgae, *Appl. Surf. Sci.*, 2020, **526**, 146538.

52 A. Shchukarev and M. Ramstedt, Cryo-XPS: probing intact interfaces in nature and life, *Surf. Interface Anal.*, 2017, **49**(4), 349–356.

53 *Introduction to near-ambient pressure x-ray photoelectron spectroscopy characterization of various materials*. Available from: **https://www.specs-group.com/nc/specsgroup/latest-news/blog/detail/introduction-to-near-ambient-pressure-x-ray-photoelectron-spectroscopy-characterization-of-various-m/**.

54 C. Guhl, P. Kehne, Q. Ma, F. Tietz, L. Alff and P. Komissinskiy, *et al.*, In-operando photoelectron spectroscopy for batteries: Set-up using pristine thin film cathode and first results on Na_xCoO_2, *Rev. Sci. Instrum.*, 2018, **89**(7), 73104.

55 S. Mandel, X-ray photoelectron spectroscopy system performs at industrially realistic pressures and temperatures. *Scilight*. 2019(41):411102. Available from: **https://aip.scitation.org/doi/abs/10.1063/10.0000137**.

56 L. Fan, J. L. Li, Z. Cai and X. Wang, Bioactive hierarchical silk fibers created by bioinspired self-assembly, *Nat. Commun.*, 2021, **12**(1), 1–9. Available from: **https://dx.doi.org/10.1038/s41467-021-22673-4**.

57 G. Y. Liu, R. Agarwal, K. R. Ko, M. Ruthven, H. T. Sarhan and J. P. Frampton, Templated Assembly of Collagen Fibers Directs Cell Growth in 2D and 3D, *Sci. Rep.*, 2017, **7**(1), 1–9.

58 F. Liu, L. Pan, Y. Liu, G. Zhai, Z. Sha and X. Zhang, *et al.*, Biobased fibers from natural to synthetic: Processing, manufacturing, and application, *Matter*, 2024, **7**(6), 1977–2010. Available from: **https://doi.org/10.1016/j.matt.2024.04.006**.

59 T. Nash, *Nature*, 1957, **180**, 188–189. Available from: **https://www.nature.com/articles/180188b0#citeas**.

60 A. Prasoon, S. Ghouse, N. N. Nguyen, H. Yang, A. Müller and C. Naisa, *et al.*, Mimicking on-water surface synthesis through micellar interfaces, *Nat. Commun.*, 2024, **15**(1), 10495. Available from: **https://dx.doi.org/10.1038/s41467-024-54962-z**.

61 Ş. Süzer, XPS investigation of X-ray-induced reduction of metal ions, *Appl. Spectrosc.*, 2000, **54**(11), 1716–1718.

62 C. Liu and A. J. Bard, Chemical redox reactions induced by cryptoelectrons on a PMMA surface, *J. Am. Chem. Soc.*, 2009, **131**(18), 6397–6401.
63 S. Piperno, H. Cohen, T. Bendikov, M. Lahav and I. Lubomirsky, The Absence of Redox Reactions for Palladium(II) and Copper(II) on Electrostatically Charged Teflon: Relevance to the Concept of ''Cryptoelectrons'', *Angew. Chemie.*, 2011, **123**(25), 5772–5775. Available from: **https://onlinelibrary.wiley.com/doi/full/10.1002/ange.201101203**.
64 S. Piperno, H. Cohen, T. Bendikov, M. Lahav and I. Lubomirsky, Absorption vs. redox reduction of Pd^{2+} and Cu^{2+} on triboelectrically and naturally charged dielectric polymers, *Phys. Chem. Chem. Phys.*, 2012, **14**(16), 5551–5557. Available from: **https://pubs.rsc.org/en/content/articlehtml/2012/cp/c2cp23000c**.
65 J. Zhang, M. L. Coote and S. Ciampi, Electrostatics and Electrochemistry: Mechanism and Scope of Charge-Transfer Reactions on the Surface of Tribocharged Insulators, *J. Am. Chem. Soc.*, 2021, **143**(8), 3019–3032.
66 S. Ray and A. G. Shard, Quantitative analysis of adsorbed proteins by X-ray photoelectron spectroscopy, *Anal. Chem.*, 2011, **83**(22), 8659–8666.
67 S. Bo, Y. Sun, S. Li, Y. Zhou, X. Feng and C. Li, Preparation of hemoglobin (Hb) imprinted polymers with CO_2 response and its biosensing application, *J. Solid State Electrochem.*, 2021, **25**(5), 1645–1655.
68 P. J. Cumpson, J. F. Portoles, A. J. Barlow, N. Sano and M. Birch, Depth profiling organic/inorganic interfaces by argon gas cluster ion beams: sputter yield data for biomaterials, in-vitro diagnostic and implant applications, *Surf. Interface Anal.*, 2013, **45**(13), 1859–1868.
69 R. Simpson, R. G. White, J. F. Watts and M. A. Baker, XPS investigation of monatomic and cluster argon ion sputtering of tantalum pentoxide, *Appl. Surf. Sci.*, 2017, **405**, 79–87.
70 H. Cohen, Towards Absolute Energy Referencing in XPS, *Surf. Interface Anal.*, 2025, **57**, 528–538.
71 D. Ehre and H. Cohen, Contact-free pyroelectric measurements using x-ray photoelectron spectroscopy, *Appl. Phys. Lett.*, 2013, **103**(5), 52901. Available from: **https://aip.scitation.org/doi/abs/10.1063/1.4817010**.
72 E. Meirzadeh, L. Sapir, H. Cohen, S. R. Cohen, D. Ehre and D. Harries, *et al.*, Nonclassical Crystal Growth as Explanation for the Riddle of Polarity in Centrosymmetric Glycine Crystals, *J. Am. Chem. Soc.*, 2016, **138**(44), 14756–14763. Available from: **https://pubs.acs.org/doi/abs/10.1021/jacs.6b09190**.
73 E. Meirzadeh, D. V. Christensen, E. Makagon, H. Cohen, I. Rosenhek-Goldian and E. H. Morales, *et al.*, Surface pyroelectricity in cubic $SrTiO_3$, *Adv. Mater.*, 2019, **31**(44), 1904733. Available from: **https://onlinelibrary-wiley-com.ezproxy.weizmann.ac.il/doi/full/10.1002/adma.201904733**.
74 H. Cohen, R. Maoz and J. Sagiv, Transient charge accumulation in a capacitive self-assembled monolayer, *Nano Lett.*, 2006, **6**(11), 2462–2466.
75 A. Vilan, T. A. Bendikov and H. Cohen, Secondary electron emission control in X-ray photoelectron spectroscopy, *J. Electron Spectrosc. Relat. Phenom.*, 2008, **162**(2), 99–105.
76 U. Korcan Demirok, G. Ertas and S. Suzer, Demirok UK, Ertas G, Suzer S. Time-resolved XPS analysis of the SiO_2/Si system in the millisecond range, *J. Phys. Chem. B*, 2004, **108**(17), 5179–5181. Available from: **https://pubs.acs.org/doi/full/10.1021/jp049526m**.
77 M. T. Camci, B. Ulgut, C. Kocabas and S. Suzer, *In Situ* XPS Monitoring and Characterization of Electrochemically Prepared Au Nanoparticles in an Ionic Liquid, *ACS Omega.*, 2017, **2**(2), 478–486. Available from: **https://pubs.acs.org/doi/abs/10.1021/acsomega.6b00456**.
78 S. K. Sarkar, G. Hodes, L. Kronik and H. Cohen, Defect-dominated charge transport in Si-supported CdSe nanoparticle films, *J. Phys. Chem. C*, 2008, **112**(16), 6564–6570.
79 S. Suzer and A. Dańa, X-ray photoemission for probing charging/discharging dynamics, *J. Phys. Chem. B*, 2006, **110**(39), 19112–19115.
80 H. Sezen, G. Ertas, A. Dâna and Ş. Süzer, Charging/discharging of thin PS/PMMA films as probed by dynamic X-ray photoelectron spectroscopy, *Macromolecules*, 2007, **40**(12), 4109–4112.
81 C. B. Uzundal, O. Sahin, P. A. Gokturk, H. Wu, F. Mugele and B. Ulgut, *et al.*, X-ray Photoelectron Spectroscopy with Electrical Modulation Can Be Used to Probe Electrical Properties of Liquids and Their Interfaces at Different Stages, *Langmuir*, 2019, **35**(52), 16989–16999.
82 D. R. Baer, M. Taner Camci, D. J. H. Cant, S. A. Chambers, H. Cohen, P. Aydogan Gokturk, D. J. Morgan, A. Shchukarev, P. M. A. Sherwood, S. Suzer, S. Tougaard and J. F. Watts, What more can be done with XPS? Highly informative but underused approaches to XPS data collection and analysis, *J. Vac. Sci. Technol. A*, 2025, **43**, 040801.
83 G. Cherkashinin, R. Hausbrand and W. Jaegermann, Performance of Li-Ion Batteries: Contribution of Electronic Factors to the Battery Voltage, *J. Electrochem. Soc.*, 2019, **166**(3), A5308–A5312.
84 T. M. Nahir, Impedance Spectroscopy: Theory, Experiment, and Applications, eds. E. Barsoukov and J. Ross Macdonald, *Journal of the American Chemical Society*, 2nd edn, John Wiley & Sons, Inc., Hoboken, NJ, 2005, vol. 127(35), p. 12431, Available from: **https://doi.org/10.1021/ja059742o**.
85 A. Lasia, Electrochemical Impedance Spectroscopy and its Applications, *Modern Aspects of Electrochemistry*, 1990, vol. 32, pp. 311–326.
86 T. R. Number, Technical report number 004/83, *Monogr. Ref.*, 1998, **4**(004), 130. Available from: **https://www.mendeley.com/research/identification-of-electrochemical-processes-by-frequency-response-analysis/**.
87 M. Brouillard, N. Bercu, U. Zschieschang, O. Simonetti, R. Mittapalli and H. Klauk, *et al.*, Experimental determination of the lateral resolution of surface electric potential measurements by Kelvin probe force microscopy using biased electrodes separated by a nanoscale gap and

application to thin-film transistors, *Nanoscale Adv.*, 2022, **4**(8), 2018–2028.

88 P. Mesquida, D. Kohl, O. G. Andriotis, P. J. Thurner, M. Duer and S. Bansode, *et al.*, Evaluation of surface charge shift of collagen fibrils exposed to glutaraldehyde, *Sci. Rep.*, 2018, **8**(1), 1–7.

89 M. Lanza, Conductive Atomic Force Microscopy: Applications in Nanomaterials, *Conductive Atomic Force Microscopy*, 2017, p. 361. Available from: **https://books.google.com/books/about/Conductive_Atomic_Force_Microscopy.html?hl=ca&id=_EozDwAAQBAJ**.

90 S. Sadewasser, P. Jelinek, C. K. Fang, O. Custance, Y. Yamada and Y. Sugimoto, *et al.*, New insights on atomic-Resolution frequency-Modulation kelvin-Probe force-Microscopy imaging of semiconductors, *Phys. Rev. Lett.*, 2009, **103**(26), 5–8.

91 Z. Qu, J. Wei, Y. Sugawara and Y. Li, Investigation of atomic surface potential on Si(111)-7 × 7 surface by high-frequency heterodyne-Kelvin probe force microscopy, *Surf. Interfaces*, 2024, **49**, 104441. Available from: **https://doi.org/10.1016/j.surfin.2024.104441**.

92 A. Sadeghi, A. Baratoff, S. A. Ghasemi, S. Goedecker, T. Glatzel and S. Kawai, *et al.*, Multiscale approach for simulations of Kelvin probe force microscopy with atomic resolution, *Phys. Rev. B: Condens. Matter Mater. Phys.*, 2012, **86**, 7.

93 E. Haviv, B. Chen, R. Carmieli, L. Houben, H. Cohen and G. Leitus, *et al.*, Guest Transition Metals in Host Inorganic Nanocapsules: Single Sites, Discrete Electron Transfer, and Atomic Scale Structure, *J. Am. Chem. Soc.*, 2020, **142**(34), 14504–14512.

94 R. Maoz, D. Burshtain, H. Cohen, P. Nelson, J. Berson and A. Yoffe, *et al.*, Site-Targeted Interfacial Solid-Phase Chemistry: Surface Functionalization of Organic Monolayers via Chemical Transformations Locally Induced at the Boundary between Two Solids, *Angew. Chem., Int. Ed.*, 2016, **55**(40), 12366–12371.

95 S. Dey, H. Cohen, I. Pinkas, H. Lin, M. Kazes and D. Oron, Band alignment and charge transfer in $CsPbBr_3$–CdSe nanoplatelet hybrids coupled by molecular linkers, *J. Chem. Phys.*, 2019, **151**(17), 174704. Available from: **https://doi.org/10.1063/1.5124552**.

96 E. Mentovich, B. Belgorodsky, M. Gozin, S. Richter and H. Cohen, Doped biomolecules in miniaturized electric junctions, *J. Am. Chem. Soc.*, 2012, **134**(20), 8468–8473.

97 E. Frydman, H. Cohen, R. Maoz, J. Sagiv, E. Frydman and H. Cohen, *et al.*, Monolayer damage in XPS measurements as evaluated by independent methods, *Langmuir*, 1997, **13**(19), 5089–5106. Available from: **https://pubs.acs.org/doi/full/10.1021/la962058q**.

98 J. Škvarla, M. Kaňuchová, A. Shchukarev, A. Girová and I. Brezáni, Cryo-XPS – A new technique for the quantitative analysis of the structure of electric double layer at colloidal particles?, *Colloids Surf., A*, 2020, **586**, 124234.

99 T. Gates, The physical and chemical ageing of polymeric composites, *Ageing Compos.*, 2008, 3–33.

100 K. Morgenstern, J. Kibsgaard, J. V. Lauritsen, E. Lægsgaard and F. Besenbacher, Cobalt growth on two related close-packed noble metal surfaces, *Surf. Sci.*, 2007, **601**(9), 1967–1972.

101 M. B. Gordon and J. Villain, The commensurate-incommensurate transition of Kr monolayers on graphite. I. Thermal expansion, *J. Phys. C: Solid State Phys.*, 1985, **18**(20), 3919. Available from: **https://iopscience.iop.org/article/10.1088/0022-3719/18/20/018**.

102 O. Seitz, A. Vilan, H. Cohen, J. Hwang, M. Haeming and A. Schoell, *et al.*, Doping molecular monolayers: effects on electrical transport through alkyl chains on silicon, *Adv. Funct. Mater.*, 2008, **18**(14), 2102–2113.

103 O. Seitz, A. Vilan, H. Cohen, C. Chan, J. Hwang and A. Kahn, *et al.*, Effect of doping on electronic transport through molecular monolayer junctions, *J. Am. Chem. Soc.*, 2007, **129**(24), 7494–7495. Available from: **https://pubs.acs.org/doi/abs/10.1021/ja071960p**.

104 R. Maoz, E. Frydman, S. R. Cohen and J. Sagiv, [a]Constructive Nanolithography[0]: Inert Monolayers as Patternable Templates for In-Situ Nanofabrication of Metal± Semiconductor ± Organic Surface Structures A Generic Approach, *Adv. Mater.*, 2000, **12**, 10.

105 *Organic monolayer nanopatterning via interfacial solid-phase electrochemical oxidation*. Available from: **https://www.hilarispublisher.com/proceedings/organic-monolayer-nanopatterning-via-interfacial-solidphase-electrochemical-oxidation-34184.html**.

106 N. Kantor-Uriel, P. Roy, K. Lerman, C. N. Sukenik and H. Cohen, Dark and photo-induced charge transport across molecular spacers, *J. Vac. Sci. Technol., B: Nanotechnol. Microelectron.: Mater., Process., Meas., Phenom.*, 2018, **36**(4), 04H104.

107 T. Aqua, H. Cohen, A. Vilan and R. Naaman, Long-range substrate effects on the stability and reactivity of thiolated self-assembled monolayers, *J. Phys. Chem. C*, 2007, **111**(44), 16313–16318.

108 *Distinction from the commonly used symbol, AL, is of no interest in the present discussion*.

109 A. Jablonski and C. J. Powell, Relationships between electron inelastic mean free paths, effective attenuation lengths, and mean escape depths, *J. Electron Spectrosc. Relat. Phenom.*, 1999, **100**(1–3), 137–160.

110 *It should be mentioned that, upon CdSe deposition, structural changes in the top T-layer took place*.

111 H. Cohen, C. Nogues, I. Zon and I. Lubomirsky, e-beam-referenced work-function evaluation in an x-ray photoelectron spectrometer, *J. Appl. Phys.*, 2005, **97**(11), 113701.

112 N. Filip-Granit, E. Goldberg, I. Samish, I. Ashur, M. E. Van Der Boom and H. Cohen, *et al.*, Submolecular gates self-assemble for hot-electron transfer in proteins, *J. Phys. Chem. B*, 2017, **121**(29), 6981–6988.

113 A. Brandis, O. Mazor, E. Neumark, V. Rosenbach-Belkin, Y. Salomon and A. Scherz, Novel Water-soluble Bacteriochlorophyll Derivatives for Vascular-targeted Photodynamic Therapy: Synthesis, Solubility, Phototoxicity and

the Effect of Serum Proteins, *Photochem. Photobiol.*, 2005, **81**(4), 983–992.

114 E. D. Mentovich, B. Belgorodsky, I. Kalifa, H. Cohen and S. Richter, Large-scale fabrication of 4-nm-channel vertical protein-based ambipolar transistors, *Nano Lett.*, 2009, **9**(4), 1296–1300.

115 E. Braun, Y. Eichen, U. Sivan and G. Ben-Yoseph, DNA-templated assembly and electrode attachment of a conducting silver wire, *Nature*, 1998, **391**(6669), 775–778.

116 K. Keren, R. S. Berman, E. Buchstab, U. Sivan and E. Braun, DNA-templated carbon nanotube field-effect transistor, *Science*, 2003, **302**(5649), 1380–1382.

117 E. Beilis, B. Belgorodsky, L. Fadeev, H. Cohen and S. Richter, Surface-induced conformational changes in doped bovine serum albumin self-assembled monolayers, *J. Am. Chem. Soc.*, 2014, **136**(17), 6151–6154.

118 H. Benyamini, A. Shulman-Peleg, H. J. Wolfson, B. Belgorodsky, L. Fadeev and M. Gozin, Interaction of C_{60}-fullerene and carboxyfullerene with proteins: docking and binding site alignment, *Bioconjugate Chem.*, 2006, **17**(2), 378–386.

119 B. Belgorodsky, L. Fadeev, J. Kolsenik and M. Gozin, Formation of a Soluble Stable Complex between Pristine C_{60}-Fullerene and a Native Blood Protein, *ChemBioChem*, 2006, **7**(11), 1783–1789.

120 E. Beilis, Y. Horowitz, A. Givon, G. A. Somorjai, H. Cohen and S. Richter, Morphology Effect on Charge Transport in Doped Bovine Serum Albumin Self-Assembled Monolayers, *J. Phys. Chem. C*, 2017, **121**(17), 9579–9586.

121 E. D. Mentovich, B. Belgorodsky, I. Kalifa and S. Richter, 1-Nanometer-Sized Active-Channel Molecular Quantum-Dot Transistor, *Adv Mater.*, 2010, **22**(19), 2182–2186. Available from: **https://onlinelibrary.wiley.com/doi/full/10.1002/adma.200902431**.

122 Under negative polarity the conduction is electron dominated (current increasing with VG), while for positive polarity it is dominated by hole transport (current decreasing upon VG increase).

123 Similar characteristics were obtained for N, with minor differences that will not be discussed here. Au-curves served as a reference - the substrate potential.

124 Alternatively, a difference in width of the two interface barriers, possibly involving a slight Pd-oxidation, could not be ruled out.

125 The 2D presentation of BSA in Fig. 14b may be insufficient to figure out the various phenyl-based hopping routes. The reader may refer to 3D presentations in the supplementary material of the original paper.

126 E. Beilis, Effect of Protein Layer Morphology Characteristics Upon Adsorption on the Layer's Charge Transport Properties, PhD thesis, Tel Aviv University, 2017.

127 S. W. Cranford and M. J. Buehler, *Biomateriomics*, Springer, 1st edn, 2012, DOI: **10.1007/978-94-007-1611-7**.

128 T. Li, V. K. Bandari and O. G. Schmidt, Molecular Electronics: Creating and Bridging Molecular Junctions and Promoting Its Commercialization, *Adv. Mater.*, 2023, **35**, 22.

129 A. Benichou, A. Aserin and N. Garti, Protein-Polysaccharide Interactions for Stabilization of Food Emulsions, *J. Dispersion Sci. Technol.*, 2002, **23**(1–3), 93–123. Available from: **https://www.tandfonline.com/doi/abs/10.1080/01932690208984192**.

130 Z. Li, H. Kuang, J. Yang, J. Hu, B. Ding and W. Sun, *et al.*, Improving emulsion stability based on ovalbumin-carboxymethyl cellulose complexes with thermal treatment near ovalbumin isoelectric point, *Sci. Rep.*, 2020, **10**(1), 1–9. Available from: **https://www.nature.com/articles/s41598-020-60455-y**.

131 M. Di Bari, A. Deriu, G. Albanese and F. Cavatorta, Dynamics of hydrated starch saccharides, *Chem. Phys.*, 2003, **292**(2–3), 333–339.

132 U. Shimanovich, D. Eliaz, I. Kellersztein, M. E. Miali, D. Benyamin and O. Brookshtein, *et al.*, Fine structural analysis of degummed fibroin fibers reveals its superior mechanical capabilities, *ChemSusChem*, 2024, 202401148.

133 G. R. Di, C. Daraio and B. Maresca, Plant nanobionic materials with a giant temperature response mediated by pectin-Ca^{2+}, *Proc. Natl. Acad. Sci. U. S. A.*, 2015, **112**(15), 4541–4545. Available from: **https://www.pnas.org/content/112/15/4541**.

134 G. R. Di, L. Bonanomi, V. Costanza, B. Maresca and C. Daraio, Biomimetic Temperature-Sensing layer for artificial skins, *Sci. Robot.*, 2017, **2**, 3.

135 Y. Feldman, A. Zak, R. Tenne and H. Cohen, Evidences for dry deintercalation in layered compounds upon controlled surface charging in x-ray photoelectron spectroscopy, *J. Vac. Sci. Technol., A.*, 2003, **21**(5), 1752–1757. Available from: **https://avs.scitation.org/doi/abs/10.1116/1.1604131**.

136 Y. Bai, Q. Luo and J. Liu, Protein self-assembly: Via supramolecular strategies, *Chem. Soc. Rev.*, 2016, **45**(10), 2756–2767.

137 A. Solomonov and U. Shimanovich, Self-Assembly in Protein-Based Bionanomaterials, *Isr. J. Chem.*, 2020, **60**(12), 1152–1170. Available from: **https://onlinelibrary.wiley.com/doi/full/10.1002/ijch.201900083**.

138 U. Shimanovich, A. Levin, D. Eliaz, T. Michaels, Z. Toprakcioglu and B. Frohm, *et al.*, pH-Responsive Capsules with a Fibril Scaffold Shell Assembled from an Amyloidogenic Peptide, *Small*, 2021, **17**(26), 2007188. Available from: **https://onlinelibrary.wiley.com/doi/full/10.1002/smll.202007188**.

139 U. Shimanovich, I. D. Tkacz, D. Eliaz, A. Cavaco-Paulo, S. Michaeli and A. Gedanken, Encapsulation of RNA Molecules in BSA Microspheres and Internalization into Trypanosoma Brucei Parasites and Human U_2OS Cancer Cells, *Adv. Funct. Mater.*, 2011, **21**(19), 3659–3666. Available from: **https://onlinelibrary.wiley.com/doi/full/10.1002/adfm.201100963**.

140 O. Brookstein, E. Shimoni, D. Eliaz, I. Kaplan-Ashiri, I. Carmel and U. Shimanovich, Metal ions guide the production of silkworm silk fibers, *Nat. Commun.*, 2024, **15**(1), 1–13. Available from: **https://dx.doi.org/10.1038/s41467-024-50879-9**.

141 M. E. Miali, D. Eliaz, A. Solomonov and U. Shimanovich, Microcompartmentalization Controls Silk Feedstock Rheology, *Langmuir*, 2023, 8984–8995.

142 H. Ibach and D. L. Mills, *Electron energy loss spectroscopy and surface vibrations*, Academic press, 2013.
143 O. L. Krivanek, T. C. Lovejoy, N. Dellby, T. Aoki, R. W. Carpenter and P. Rez, *et al.*, Vibrational spectroscopy in the electron microscope, *Nature*, 2014, **514**(7521), 209–212.
144 A. Howie and R. H. Milne, Excitations at interfaces and small particles, *Ultramicroscopy*, 1985, **18**(1–4), 427–433.
145 T. L. Ferrell and P. M. Echenique, Generation of Surface Excitations on Dielectric Spheres by an External Electron Beam, *Phys. Rev. Lett.*, 1985, **55**(14), 1526. Available from: **https://journals.aps.org/prl/abstract/10.1103/PhysRevLett.55.1526**.
146 R. J. Warmack, R. S. Becker, V. E. Anderson, R. H. Ritchie, Y. T. Chu and J. Little, *et al.*, Surface-plasmon excitation during aloof scattering of low-energy electrons in micropores in a thin metal foil, *Phys. Rev. B: Condens. Matter Mater. Phys.*, 1984, **29**(8), 4375. Available from: **https://journals.aps.org/prb/abstract/10.1103/PhysRevB.29.4375**.
147 H. Cohen, T. Maniv, R. Tenne, Y. R. Hacohen, O. Stephan and C. Colliex, Near-field electron energy loss spectroscopy of nanoparticles, *Phys. Rev. Lett.*, 1998, **80**(4), 782. Available from: **https://journals.aps.org/prl/abstract/10.1103/PhysRevLett.80.782**.
148 R. Walther, S. Fritz, E. Müller, R. Schneider, D. Gerthsen and W. Sigle, *et al.*, Coupling of surface-plasmon-polariton-hybridized cavity modes between submicron slits in a thin gold film, *ACS Photonics*, 2016, **3**(5), 836–843. Available from: **https://pubs.acs.org/doi/abs/10.1021/acsphotonics.6b00045**.
149 P. Rez, T. Aoki, K. March, D. Gur, O. L. Krivanek and N. Dellby, *et al.*, Damage-free vibrational spectroscopy of biological materials in the electron microscope, *Nat. Commun.*, 2016, **7**(1), 1–8. Available from: **https://www.nature.com/articles/ncomms10945**.
150 A. Barth, The infrared absorption of amino acid side chains, *Prog. Biophys. Mol. Biol.*, 2000, **74**(3–5), 141–173.
151 Normally, core electron orbitals are negligibly altered upon chemical bond formation and the effect of valence electrons redistribution is restricted to a shift in their energy. For hydrogen, the only electron to be probed is a valence electron.
152 N. Aggarwal, D. Eliaz, H. Cohen, I. Rosenhek-Goldian, S. R. Cohen and A. Kozell, *et al.*, Protein nanofibril design via manipulation of hydrogen bonds, *Commun. Chem.*, 2021, **4**(1), 1–10. Available from: **https://dx.doi.org/10.1038/s42004-021-00494-2**.
153 H. Alpern, K. Yavilberg, T. Dvir, N. Sukenik, M. Klang and S. Yochelis, *et al.*, Magnetic-related states and order parameter induced in a conventional superconductor by nonmagnetic chiral molecules, *Nano Lett.*, 2019, **19**(8), 5167–5175. Available from: **https://pubs.acs.org/doi/abs/10.1021/acs.nanolett.9b01552**.